Simulation study of Cornell L0 beamline

Tsukasa MIYAJIMA*
Accelerator laboratory,
High Energy Accelerator Research Organization (KEK),
1-1 Oho, Tsukuba, Ibaraki 305-0801, Japan

Ivan V. Bazarov
Cornell University, Ithaca, NY 14853, USA

August 27, 2010

1 Injector simulation

To generate high quality synchrotron radiation in the future ERL light sources, the performance of the ERL injector, which has critical components, a photo cathode gun and super conducting cavities, is very important. In the injector, an electron beam is generated by photo cathode DC gun, and accelerated by super conducting RF cavities. Since an electron beam with -77 pC bunch charge and 1.3 GHz repetition rate has lower energy less than 15 MeV in the injector, space charge effect plays an important role in emittance compensation. The quality of electron beam depends on initial laser pulse, magnetic field of solenoid magnets and time dependent electromagnetic field in RF cavities. To generate high quality electron beam, these parameters are optimized using particle tracking simulation with space charge effect and multi objective method [1]. To obtain the minimum emittance at the exit of ERL injector beam line, beam simulations were carried using particle tracking code, Astra [2]. In this report, the optimization results to minimize normalized rms emittance and rms bunch length at the exit of injector are described.

In this report, the components and field maps, which are in the injector beam line, are described in section 1.1. The initial particle distribution and optimization method are described in section 1.2 and 1.3, respectively. The optimization results are shown in section 1.4. Finally, the summary of the optimization is described in section 1.5.

*E-mail address: tsukasa.miyajima@kek.jp

1.1 Layout and field maps of L0 beamline

The L0 beamline have been constructed in Cornell University to study ERL injector. The L0 beamline consists of photo cathode DC gun (GA1GHV01), two solenoid magnets (MA1SLA01 and MA1SLA01), buncher cavity (RA1CTB01), five super conducting RF cavities (RA2CTC01-RA2CTC05), fourth quadrupole magnets (MA3QUA01- MA3QUA04). A straight section, a chicane section and a merger section are connected behind the fourth quadrupole magnets in the A3 section. The location of elements in L0 beam line from A1 to A3 section is shown in Table 1.

Figure 1 shows the cross section of the DC photo cathode gun. The maximum voltage of the gun is 750 kV. The one dimensional field map of the DC gun calculated by Poisson Superfish is shown in Fig. 2. The cathode has a Pierce-type electrode, which have the focusing angle of 25 degree. Since the shape of the electrode has cylindrical symmetry, the transverse electric field is calculated from the longitudinal electric field,

$$E_r(r,z) = -\frac{1}{2} r \frac{\partial E_z}{\partial z}|_{r=0}. \tag{1}$$

Since $\partial E_z/\partial z < 0$ around the cathode surface as shown in Fig. 2, the transverse electric field causes focusing force. Figure 3 shows the cross section of the solenoid magnet. One dimensional field map of the solenoid magnet is shown in Fig. 4. Since the solenoid magnet has cylindrical symmetry, the transverse magnetic field is calculated by

$$B_r(r,z) = -\frac{1}{2} r \frac{\partial B_z}{\partial z}|_{r=0}. \tag{2}$$

The emittance, which is increased by space charge effect after the gun, is compensated by the solenoid magnetic field. Figure 5 shows the one dimensional field map of the bunching cavity, RA1CTB01. Figures 6 and 7 show the one dimensional field map of the 2-cell super conducting RF cavity with input coupler at the entrance and exit of the cavity, respectively. The electromagnetic field of the RF cavity with cylindrical symmetry is calculated by

$$\begin{aligned} E_z(r,z,t) &= E_z(z)\cos(\omega t + \phi), & (3)\\ E_r(r,z,t) &= -\frac{1}{2} r \frac{\partial E_z}{\partial z}|_{r=0} \cos(\omega t + \phi), & (4)\\ B_\phi(r,z,t) &= \frac{r\omega}{2c^2} E_z(z)\sin(\omega t + \phi). & (5) \end{aligned}$$

Since the electromagnetic field depends on time, the electron beam with finite bunch length is affected by the time dependent focusing effect in the RF cavity. The strength and phase of the electromagnetic field in the RF cavity must be adjusted to obtain the minimum emittance.

In the simulation, emittance and bunch length at the A4 slit, which is located on 9.5 m from the cathode surface, were calculated using the above field maps.

Element	Element name	Position, z (m)
DC gun	GA1GHV01	0
First solenoid	MA1SLA01	0.303
Bunching cavity	RA1CTB01	0.714
Second solenoid	MA1SLA02	1.128
First SRF cavity	RA2CTC01	2.047
Second SRF cavity	RA2CTC02	2.833
Third SRF cavity	RA2CTC03	3.696
Fourth SRF cavity	RACTC04	4.482
Fifth SRF cavity	RACTC05	5.345
First quadrupole magnet	MA3QUA01	6.5421
Second quadrupole magnet	MA3QUA02	7.1421
Third quadrupole magnet	MA3QUA03	7.7421
Fourth quadrupole magnet	MA3QUA04	8.3421

Table 1: Location of elements in L0 beam line from A1 to A3 section.

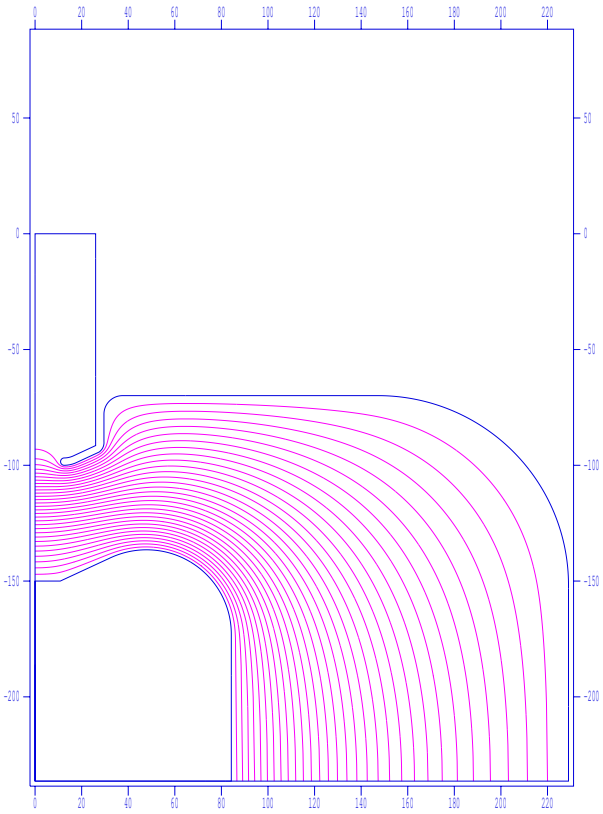

Figure 1: Cross section of photo cathode DC gun. The horizontal axis is radial coordinate. The vertical axis is longitudinal coordinate.

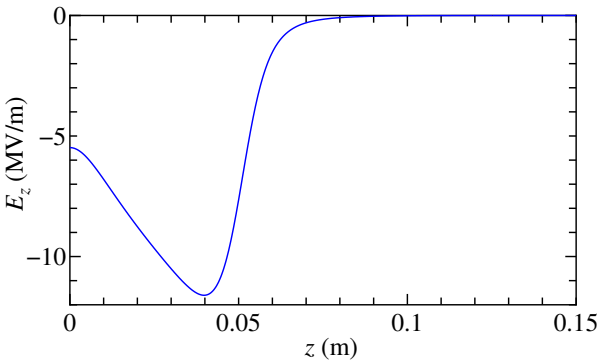

Figure 2: One dimensional field map of photo cathode DC gun. The horizontal axis is longitudinal distance from cathode surface. The vertical axis is electric field strength along the longitudinal coordinate with the voltage of 500 kV.

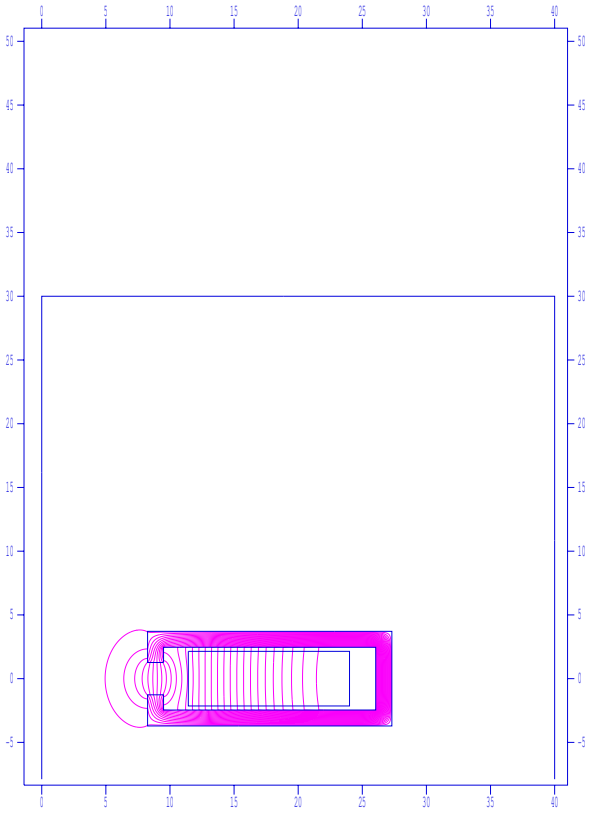

Figure 3: Cross section of solenoid magnet. The horizontal axis is radial coordinate. The vertical axis is longitudinal coordinate.

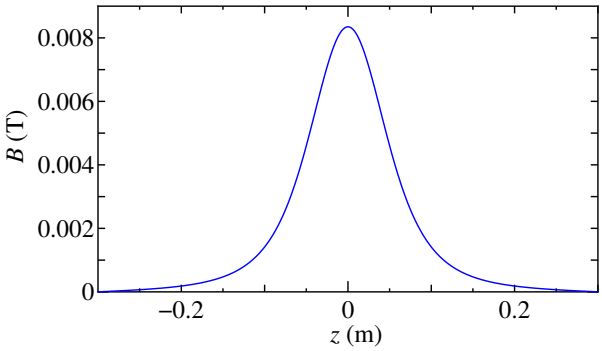

Figure 4: One dimensional field map of solenoid magnet. The horizontal axis is longitudinal coordinate. The vertical axis is the longitudinal component of the magnetic field.

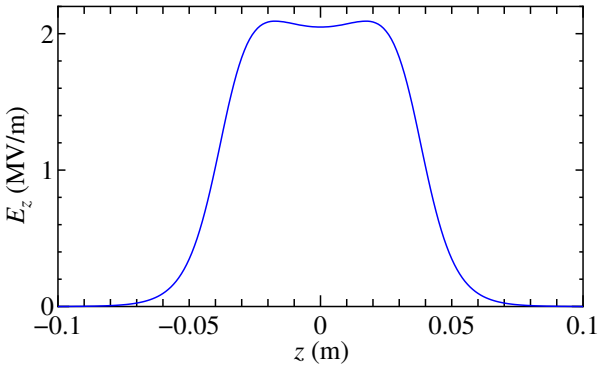

Figure 5: One dimensional field map of bunching cavity. The horizontal axis is longitudinal coordinate. The vertical axis is the longitudinal component of electric field.

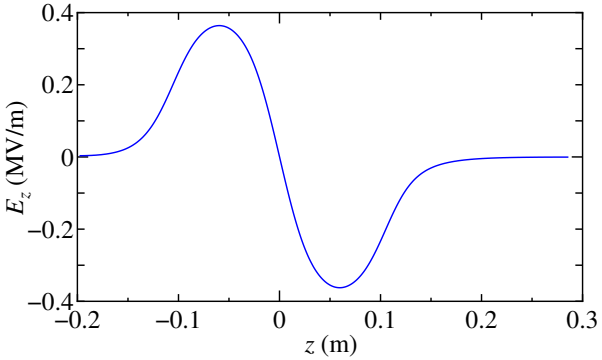

Figure 6: One dimensional field map of 2-cell super conducting RF cavity. The input coupler is located to the entrance of the cavity. The horizontal axis is longitudinal coordinate. The vertical axis is the longitudinal component of electric field.

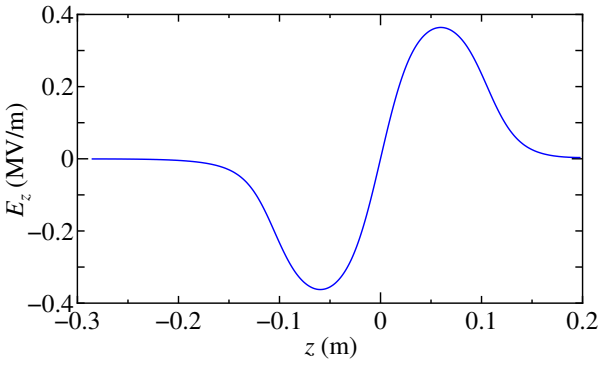

Figure 7: One dimensional field map of 2-cell super conducting RF cavity. The input coupler is located to the exit of the cavity. The horizontal axis is longitudinal coordinate. The vertical axis is the longitudinal component of electric field.

1.2 Initial particle distribution

In the simulation, the beer-can distribution is used as an initial particle distribution. The beer-can distribution has radial uniform distribution on x-y space and uniform distribution in time. Figure 8 shows initial particle distribution with beer-can shape. The particle distribution on momentum space is shown in Fig. 9. The distribution is generated by Astra code. To generate beer-can distribution of electron beam, laser pulse stacking and shaping are used. However, actual cathode has non-zero response time. Thus, the finite response time causes the tail of the electron distribution. Here, it assumes that the cathode has zero response time to estimate the minimum emittance in the beamline.

The electron beam immediately after generation has non-zero initial emittance. It depends on the properties of the cathode and the laser, e.g. cathode width, wave length of laser, band gap and quantum efficiency. In the simulation, it assumes that the initial thermal energy of the beam, k_BT is 100 or 150 meV. The initial emittance can be calculated by

$$\epsilon_{nx} = \sigma_{x0}\sqrt{\frac{k_BT}{mc^2}}. \tag{6}$$

The particle distribution in the transverse momentum space is shown in Figure 9. The distribution is radial Gaussian. In addition, it assumes that the longitudinal momentum of the initial distribution is zero, $p_z = 0$.

1.3 Simulation and optimization of beamline parameters

In the simulation, Astra was used as a particle tracking code with space charge effect. Astra includes space charge calculation based on cylindrical two dimensional mash method. The mesh size in the space charge calculation affects the calculation results. Larger mesh size improves the accuracy of the calculated results. However, larger mesh size increases CPU time. Thus,

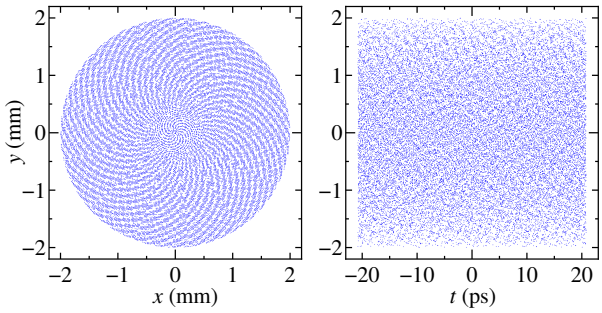

Figure 8: Initial distribution of injector simulation. The left graph shows the x-y distribution. The right graph shows the temporal distribution.

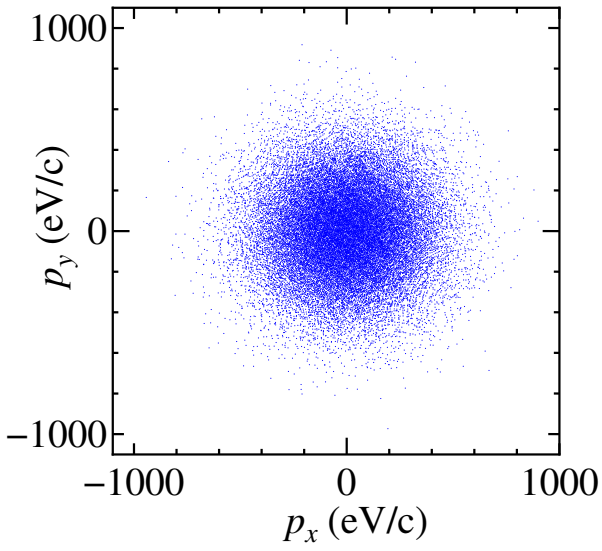

Figure 9: Initial distribution of injector simulation in transverse momentum space.

Variable	range
Initial laser pulse width, σ_{t0}	0 to 30 ps
Initial laser rms size, σ_{x0}	0 to 2 mm
Maximum Ez of RA1CTB01	0 to 10 MV/m
Maximum Ez of RA1CTC01	10 to 30 MV/m
Maximum Ez of RA1CTC02	10 to 30 MV/m
Maximum Ez of RA1CTC03-5	10 to 30 MV/m
Phase, ϕ of RA1CTC01	-60 to 10 degree
Phase, ϕ of RA1CTC02	-60 to 10 degree
Phase, ϕ of RA1CTC03-5	-30 to 20 degree
Maximum B_z of MA1SLA01	0 to 0.1 T
Maximum B_z of MA1SLA02	0 to 0.1 T

Table 2: Variables in optimization.

there is optimum mesh size for number of macro particles. The optimum mesh size is the radial size of 35 and the longitudinal size of 75 for 28 k particles. In the simulation, the above mesh parameters were used.

The simulations were carried out using Astra version 3.0, 1.0 and 1.1. Astra version 3.0 was developed by DESY, Hamburg 1999-2002, version 1.0 was developed in 2002, and version 1.1 was developed in 2007. In order to check the difference between these versions, three simulations were carried. In optimization of the beamline parameters, version 3.0 was mainly used.

To optimize the beamline parameters, parameter optimizations were carried using multi objective method. In the optimization, emittance and rms bunch length at the A4 slit were minimized with constraints of parameters. The following parameters were varied in the optimization. The ranges of variables are shown in Table 2. In the optimization, the calculated parameters were restricted as shown in Table 3 to obtain realistic results.

The optimization was carried out with the following two steps. In the first step, the number of particles in the simulation was 1 k macro particles to reduce CPU time and to obtain rough results. In the second step, the number of particles was 28 k particles to obtain more accurate results, and the result with 1 k macro particles refers as the initial optimization condition.

1.4 simulation results

The optimizations to minimize normalize rms emittance and bunch length at the A4 slit were carried out using cluster linux computer system. Figure 10 shows the optimization results with initial $k_BT = 100$ meV. The gun voltage varied from 350 kV to 750 kV. The dashed lines in

Constraint	condition
Rms beam size, σ_x	< 2.0 mm
Rms bunch length, σ_z	< 0.25 mm
Rms energy spread, $\sigma_{\Delta E}$	$-150 < \sigma_{\Delta E} < 150$ keV
Normalized rms emittance, ϵ_{nx}	< 2.0 mm mrad

Table 3: Constraints of optimization at A4 slit.

Fig. 10 are possible minimum emittances calculated by

$$\epsilon_{nx} \geq 4\sqrt{QE_{th}/E_{cath}}. \tag{7}$$

Here, Q is the bunch charge (nC), E_{th} is k_BT, (eV), and E_{cath} is the longitudinal electric field on the cathode surface (MV/m). Figure 10 shows that in proportion as the increase of the gun voltage the emittance decreases. For the gun voltage of 350 kV, the difference between the calculated emittance and the possible minimum is larger than for the result for 750 kV. The emittance growth is caused by space charge effect between the gun and the SRF cavity. Thus, to reduce the emittance growth, the gun voltage is extremely important. For the gun voltage of 750 kV, the minimum emittance approaches possible minimum emittance. The electron beam with longer bunch length has smaller emittance as shown in Fig. 10. Since the effect of time dependent RF field and the density of charge become smaller for the electron beam with shorter bunch length, the emittance growth through the RF focusing and space charge effect become smaller. The emittance growth immediately increases, when the bunch length is less than 0.3 mm as shown in Fig. 10.

Figure 11 shows the effect of the initial thermal energy on the cathode. For 350 and 500 kV, the difference of the emittance between 100 and 150 meV is not so large. On the other hand, the electron beam with 150 meV for 750 kV has larger emittance compared with the results with 100 meV. Figure 12 shows the rms transverse beam size with $k_BT = 100$ meV at A4 slit. The horizontal axis is same as Fig. 10. The transverse beam size at A4 slit is distributed from 0.2 to 0.7 mm. Figure 13 shows the kinetic energy and rms energy spread with $k_BT = 100$ meV at A4 slit. The kinetic energy and the energy spread are distributed from 10 to 11 MeV, and from 10 to 130 keV, respectively.

The optimized beamline parameters are shown in Figures 14-17. Figure 14 shows the initial laser pulse width and rms beam size for optimization results with $k_BT = 100$ meV. As shown in Fig. 14, the result with lower gun voltage has shorter initial laser pulse width, and larger initial laser spot size. Figure 15 shows that the solenoid strengths do not depend on the bunch length at A4 slit, and the result with higher gun voltage have stronger solenoid field. The higher electric field of the bunching cavity is required for higher gun voltage as shown in Fig. 16. On

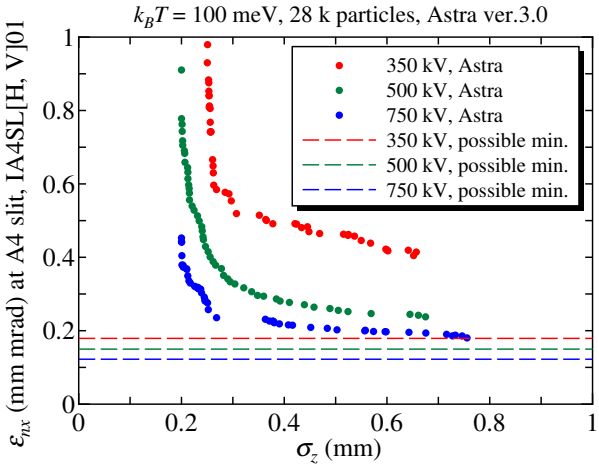

Figure 10: Optimization results with initial $k_BT = 100$ meV. The horizontal and vertical axes are bunch length and normalized rms emittance at A4 slit, respectively. The dashed lines show possible minimum emittances calculated by Eq. (7).

the other hand, the lower electric field of the first SRF cavity is required for high gun voltage. Figure 17 shows that in proportion as the increase of the bunch length the phase of the first SRF cavity increases, and it does not depend on the gun voltage. The phase of second cavity is almost -60 degree. These results show that the phase of SRF cavity is important to adjust the RF focusing effect.

The time evolutions of the beam parameters for the bunch length of 0.6 mm at the A4 slit with the gun voltage of 500 kV are calculated using Astra ver. 3.0, 1.0 and 1.1, and the results are shown in Figs. 18, 19 and 20, respectively. The beamline parameters are selected from the optimization results, and shown in Table 4. Table 5, 6 and 7 show the beam parameters at the A4 slit calculated by Astra ver. 3.0, 1.0 and 1.1. Figure 21 shows that the differences of the beam parameter calculated by the different versions of Astra. The transverse emittance calculated by ver. 3.0 has different time evolution from ones calculated by ver. 1.0 and 1.1. For the longitudinal emittance, the result of ver. 3.0 is larger than ones of ver. 1.0 and 1.1. For the other parameters, every version of Astra has almost same results. Table 8 shows the calculated results at the A4 slit by Astra ver. 3.0, 1.0 and 1.1. It shows the difference of the result is not so larger for the optimization work.

From the optimization results, the minimum emittances with 0.6 mm bunch length were estimated to be 0.43 mm mrad for 350 kV, 0.26 mm mrad for the gun voltage of 500 kV, and 0.21 mm mrad for 750 kV as shown in Table 7. In this case, the kinetic energy is about 10 MeV.

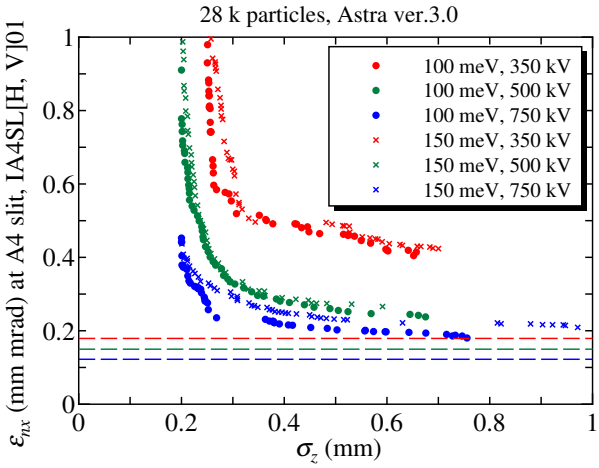

Figure 11: Optimization results with initial k_BTs of 100 and 150 meV. The horizontal and vertical axes are bunch length and normalized rms emittance at A4 slit, respectively.

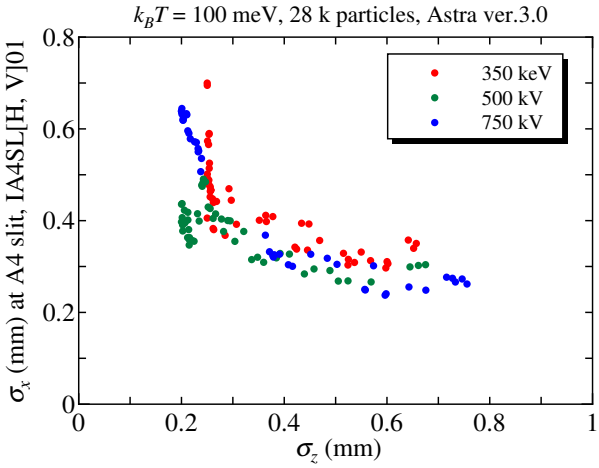

Figure 12: Rms beam size with $k_BT = 100$ meV at A4 slit. The horizontal axis is same as Fig. 10.

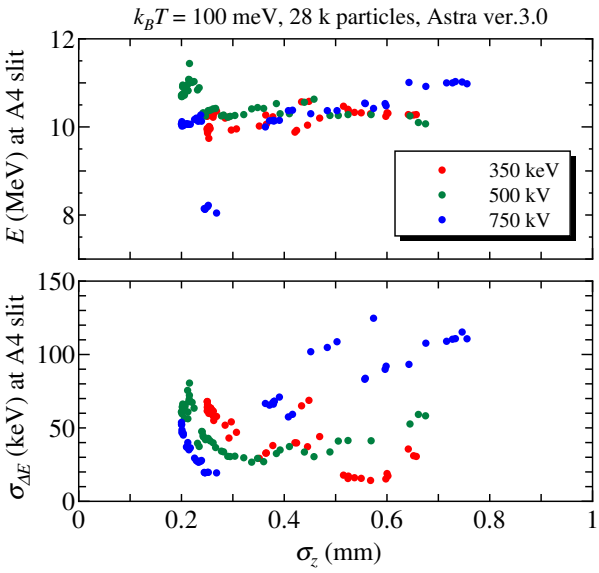

Figure 13: Kinetic energy and rms energy spread with $k_BT = 100$ meV at A4 slit. The horizontal axis is same as Fig. 10.

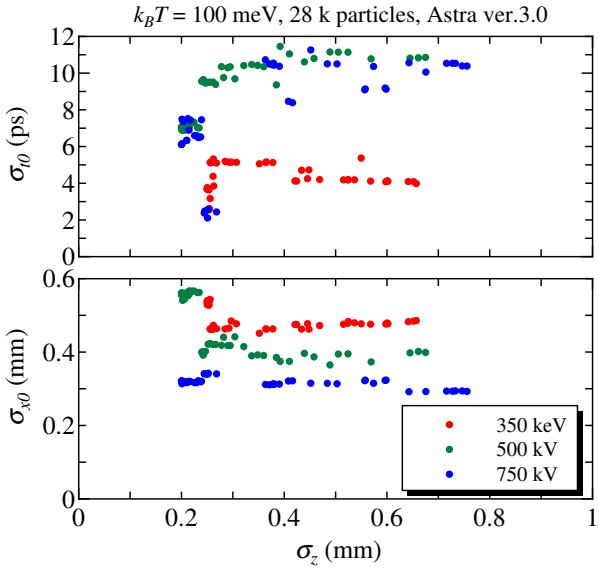

Figure 14: Initial laser pulse width and rms beam size for optimization results with $k_BT = 100$ meV. The horizontal axis is same as Fig. 10. The upper graph shows initial laser width. The lower graph shows the transverse rms laser spot size.

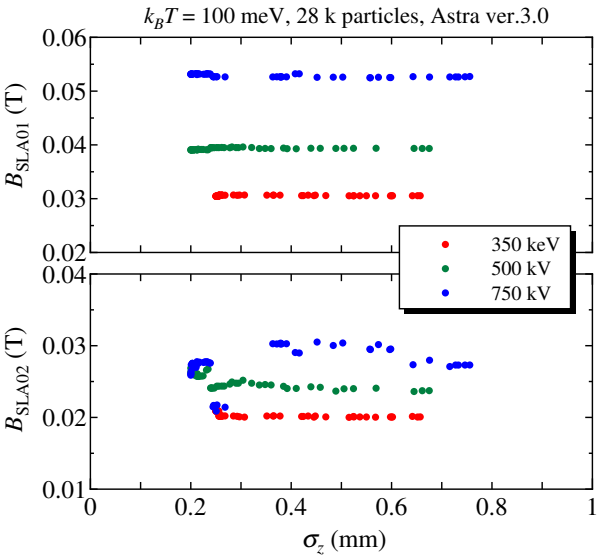

Figure 15: Solenoid strengths. The horizontal axis is same as Fig. 10.

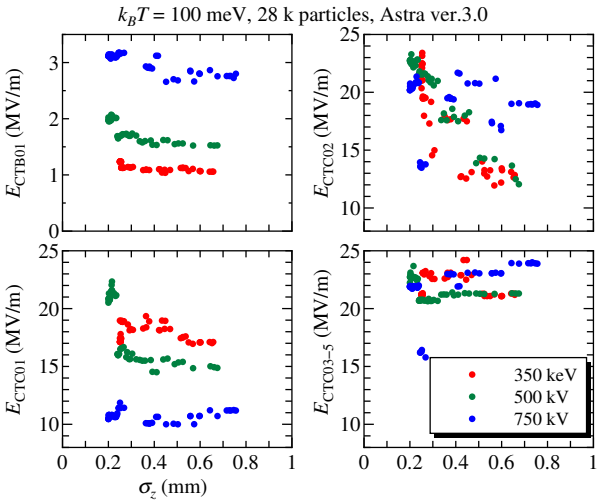

Figure 16: Electric fields of RF cavities. The horizontal axis is same as Fig. 10.

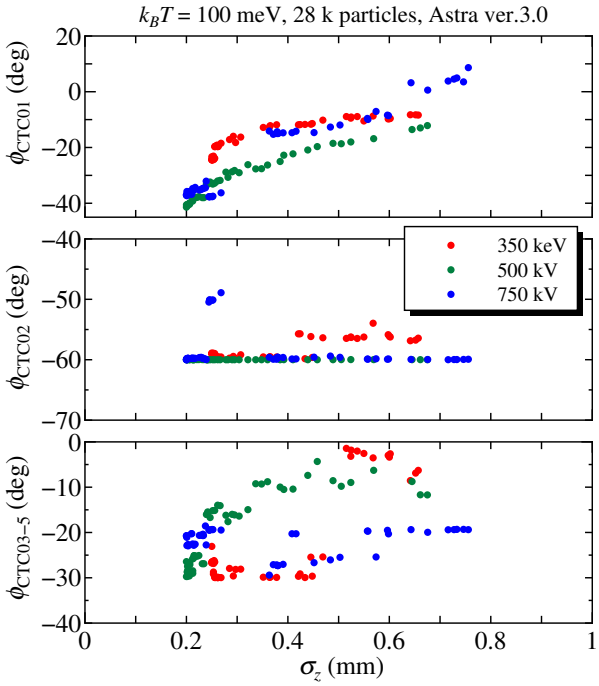

Figure 17: RF phase difference of RF cavities. The horizontal axis is same as Fig. 10. When the phase difference is zero, the cavity gives maximum acceleration.

Variable	350 kV	500 kV	750 kV
Initial laser pulse width, σ_{t0} (ps)	4.12818	10.7805	9.12441
Initial laser rms size, σ_{x0} (mm)	0.479323	0.373222	0.323536
Maximum Ez of RA1CTB01 (MV/m)	1.06711	1.52283	2.79892
Maximum Ez of RA1CTC01 (MV/m)	17.0912	14.85	10.7251
Maximum Ez of RA1CTC02 (MV/m)	13.4257	14.2251	16.7352
Maximum Ez of RA1CTC03-5 (MV/m)	21.0904	21.2751	23.0617
Phase, ϕ of RA1CTC01 (degree)	−9.66067	−16.833	−8.5645
Phase, ϕ of RA1CTC02 (degree)	−56.1217	−59.9792	−59.8713
Phase, ϕ of RA1CTC03-5 (degree)	−3.36892	−6.27835	−20.308
Maximum Bz of MA1SLA01 (T)	0.0305504	0.0393791	0.0525231
Maximum Bz of MA1SLA02 (T)	0.0200574	0.024076	0.0295408

Table 4: Optimized beamline parameters with bunch length of 0.6 mm at A4 slit.

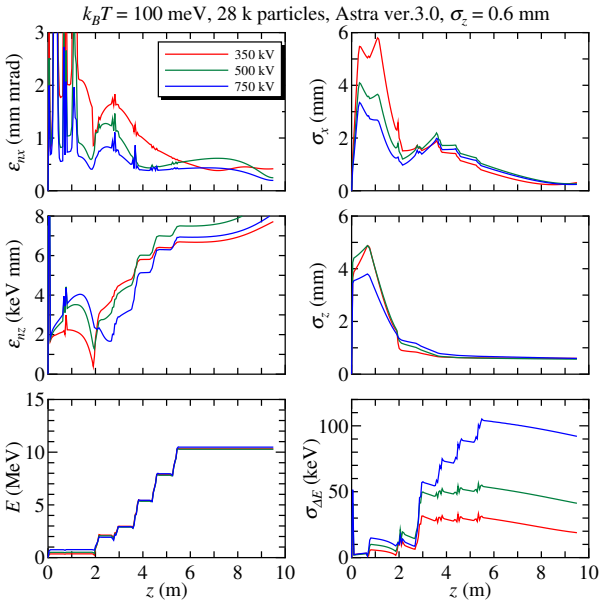

Figure 18: Time evolutions of beam parameters calculated by Astra ver. 3.0. The bunch length at A4 slit is 0.6 mm.

Value	350 kV	500 kV	750 kV
ϵ_{nx} (mm mrad)	0.4169	0.2466	0.1963
σ_x (mm)	0.3095	0.2664	0.2406
ϵ_{nz} (keV mm)	7.720	9.146	8.129
σ_z (mm)	0.6001	0.5691	0.5983
E (MeV)	10.32	10.28	10.48
$\sigma_{\Delta E}$ (keV)	18.91	41.25	92.05

Table 5: Calculated results with 0.6 mm bunch length at A4 slit by Astra ver. 3.0.

Value	350 kV	500 kV	750 kV
ϵ_{nx} (mm mrad)	0.39428	0.23337	0.19120
σ_x (mm)	0.31016	0.26984	0.24353
ϵ_{nz} (keV mm)	6.1564	7.9129	6.7262
σ_z (mm)	0.60996	0.57020	0.59937
E (MeV)	10.316	10.273	10.472
$\sigma_{\Delta E}$ (keV)	20.010	43.088	93.358

Table 6: Calculated results with 0.6 mm bunch length at A4 slit by Astra ver. 1.0.

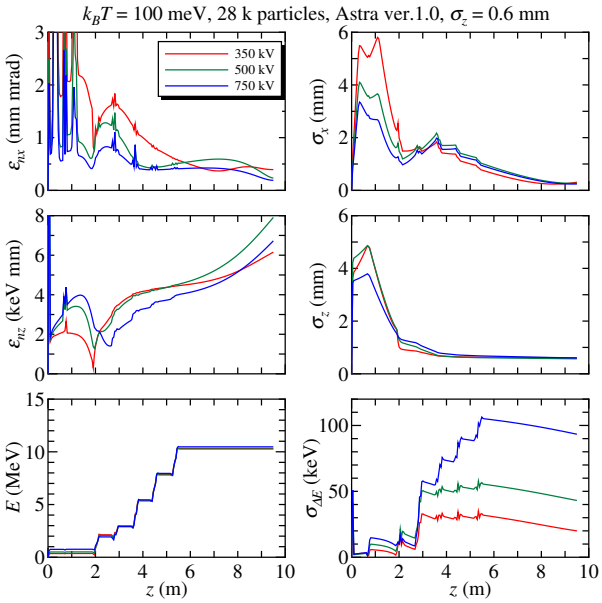

Figure 19: Time evolutions of beam parameters calculated by Astra ver. 1.0. The bunch length at A4 slit is 0.6 mm.

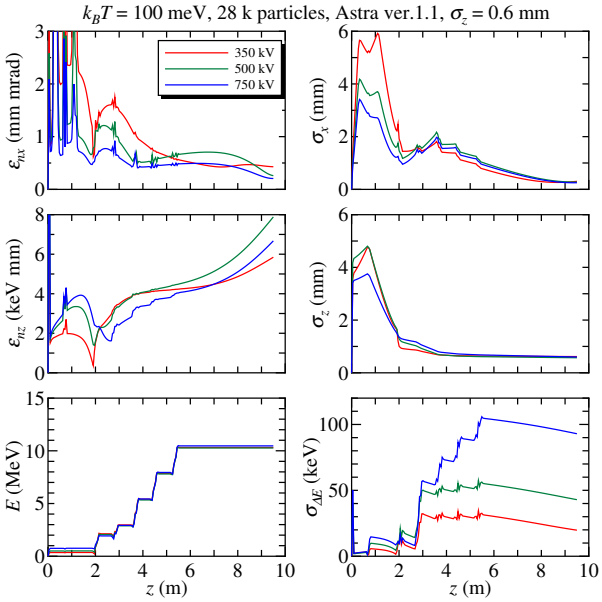

Figure 20: Time evolutions of beam parameters calculated by Astra ver. 1.1. The bunch length at A4 slit is 0.6 mm.

Value	350 kV	500 kV	750 kV
ϵ_{nx} (mm mrad)	0.42910	0.26070	0.20709
σ_x (mm)	0.30617	0.28042	0.25228
ϵ_{nz} (keV mm)	5.8474	7.8860	6.6752
σ_z (mm)	0.61651	0.57258	0.60048
E (MeV)	10.315	10.271	10.469
$\sigma_{\Delta E}$ (keV)	19.775	42.928	92.967

Table 7: Calculated results with 0.6 mm bunch length at A4 slit by Astra ver. 1.1.

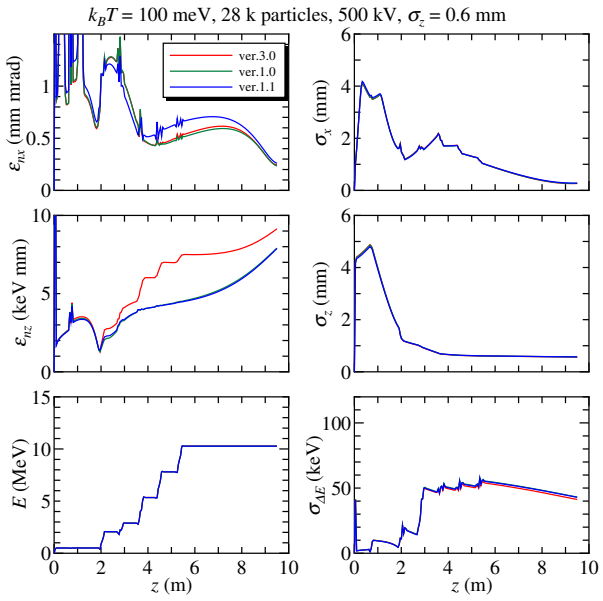

Figure 21: Time evolutions of beam parameters calculated by Astra ver. 3.0, 1.0 and 1.1. The DC gun voltage and the bunch length at A4 slit are 500 kV and 0.6 mm, respectively.

Value	Astra ver. 3.0	Astra ver. 1.0	Astra ver 1.1
ϵ_{nx} (mm mrad)	0.2466	0.23337	0.26070
σ_x (mm)	0.2664	0.26984	0.28042
ϵ_{nz} (keV mm)	9.146	7.9129	7.8860
σ_z (mm)	0.5691	0.57020	0.57258
E (MeV)	10.28	10.273	10.271
$\sigma_{\Delta E}$ (keV)	41.25	43.088	42.928

Table 8: Calculated results with 500 kV gun voltage and 0.6 mm bunch length at A4 slit by Astra ver. 3.0, 1.0 and 1.1.

1.5 Summary

In order to optimize parameters in L0 injector beamline, the particle tracking simulations were carried out using particle tracking code, Astra, which has mesh based space charge calculation. The emittance and the rms bunch length at the A4 slit were minimized in the optimizations. From the optimization results, the minimum emittances with 0.6 mm bunch length were estimated to be 0.43 mm mrad for 350 kV, 0.26 mm mrad for the gun voltage of 500 kV, and 0.21 mm mrad for 750 kV. The kinetic energy is about 10 MeV. In proportion as the increase of the gun voltage the emittance approaches possible minimum emittance, which depends on the bunch charge and the electric field strength on the cathode surface. The results show that the gun voltage is extremely important to decrease emittance.

2 Emittance growth in merger section

In order to merge the electron beam from the injector to the return loop section, a merger section is connected behind the injector. The merger section consists of three bending magnets , two quadrupole magnets and drift spaces. Since the dispersion function in the merger section is not zero, emittance growth is caused by coupling it and longitudinal space charge force. In this section, to estimate the emittance growth in the merger section, beam dynamics simulations were carried out for the three different types of mergers. The beamline consists the merger and main SRF cavities. As the particle tracking code, GPT [3] was used. GPT can calculate space charge effect not only in straight section but also in bending magnet.

2.1 Layouts of merger

In this study, we calculate beam dynamics in three different types of merger. The first merger consists of three dipole magnets and two quadrupole magnets with the injection angle of 15 degree. It is used in L0 project, which is ERL test project in Cornell University. In this paper, we call it 'L0B1 merger'. Table 9 shows the parameters of the bending magnets in the L0B1 merger. The fringe field parameter, b_1, is calculated by

$$b_1 = \frac{1}{2 \cdot \mathrm{HGAP} \cdot \mathrm{FINT}}, \tag{8}$$

where HGAP and FINT are half of magnet pole gap and the parameter of edge-field integral in `elegant`. Table 10 shows the parameters of the quadrupole magnets in the L0B1 merger. The second merger consists of four dipole magnets with the injection angle of 15 degree. It is used in test ERL beamline in BNL and called 'zigzag merger'. Table 11 shows the parameters of the bending magnets in the zigzag merger. The final beamline have a pure drift space before the first super conducting cavity (SRF1). The drift length is same as the lengths of L0B1 and zigzag mergers. The beamline is useful to compare the emittance growth in the mergers. The layouts of the mergers are shown in Fig. 22. Figure 23 shows the one dimensional electric field of the SRF cavity. The locations of SRF cavities are shown in Table 12.

2.2 Courant-Snyder parameters in merger section

Before particle tracking simulations with space charge effect, the Courant-Snyder parameters in merger section, which are calculated by GPT, are compared with linear optics calculated by `elegant` to confirm the input files for GPT.

In the particle tracking simulation, the particle motion is described by six-dimensional parameters, $(x, y, z, \dot{x}, \dot{y}, \dot{z})$, where $\dot{x}$ denotes dx/dt. Usually, the electron bunch is described by macro particles in the particle tracking with space charge effect. The rms or average beam parameters are calculated from the particle distribution, which consists of N macro particles.

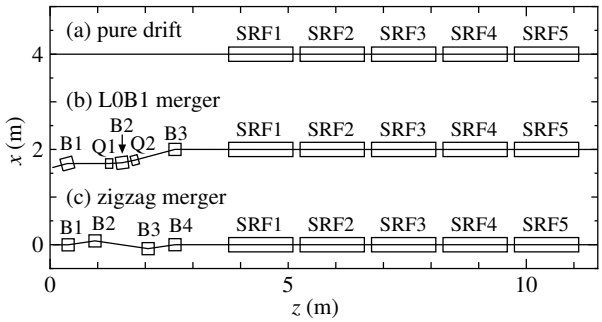

Figure 22: Layouts of beamlines with (a) pure drift, (b) L0B1 merger and (c) zigzag merger before super conducting cavity. These beamlines have same longitudinal length from start point to the entrance of first SRF cavity (SRF1). The field map of the SRF cavity is shown in Fig 23.

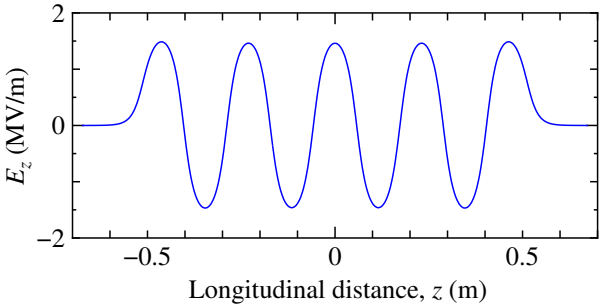

Figure 23: Longitudinal one-dimensional electric field map for 9-cells super conducting cavity.

Element name	s_{in} (m)	L (m)	R_B (m)	θ_B (degree)	b_1 (m^{-1})
B1	0.2	0.254	0.98	−15	40
B2	1.349	0.254	0.98	15	40
B3	2.491	0.254	0.98	−15	40

Table 9: Parameters of bending magnets in L0 merger. s_{in} is the position on the entrance of the magnet along reference orbit, L is the length of the rectangular magnet, R_B is the bending angle, θ_B is the bending angle, and b_1 is the parameter for fringe field. The total length of the merger is 2.55 m.

Element	Element name	s_{in} (m)	L (m)
First quadrupole magnet	Q1	1.203	0.151
Second quadrupole magnet	Q2	1.750	0.151

Table 10: Parameters of quadrupole magnets in L0B1 merger. s_{in} is the position on the entrance of the magnet along reference orbit, and L is the length of the magnet.

Element name	s_{in} (m)	L (m)	R_B (m)	θ_B (degree)	b_1 (m^{-1})
B1	0.2	0.254	0.98	15	40
B2	0.709	0.254	0.98	-30	40
B3	1.892	0.254	0.98	30	40
B4	2.576	0.254	0.98	-15	40

Table 11: Parameters of bending magnets in zigzag merger. s_{in} is the position on the entrance of the magnet along reference orbit, L is the length of the rectangular magnet, R_B is the bending angle, θ_B is the bending angle, and b_1 is the parameter for fringe field. The total length of merger is 2.55 m.

Element	Element name	Position, s (m)
First SRF cavity	ECTE01	4.425
Second SRF cavity	ECTE02	5.925
Third SRF cavity	ECTE03	7.425
Fourth SRF cavity	ECTE04	8.925
Fifth SRF cavity	ECTE05	10.425

Table 12: Locations of SRF cavities in beam line from entrance of merger.

From the particle distribution, the Courant-Snyder (CS) parameters are defined by

$$\alpha_{x,cs} = -\frac{\langle\gamma\rangle\langle x_c\beta_{xc}\rangle}{\epsilon_{nx}}, \tag{9}$$

$$\beta_{x,cs} = \frac{\langle\gamma\rangle\langle\beta_z\rangle\langle x_c^2\rangle}{\epsilon_{nx}}, \tag{10}$$

$$\alpha_{y,cs} = -\frac{\langle\gamma\rangle\langle y_c\beta_{yc}\rangle}{\epsilon_{ny}}, \tag{11}$$

$$\beta_{y,cs} = \frac{\langle\gamma\rangle\langle\beta_z\rangle\langle y_c^2\rangle}{\epsilon_{ny}}, \tag{12}$$

where ϵ_{nx} and ϵ_{ny} are horizontal and vertical normalized rms emittances, $\langle\rangle$ denotes average for macro particles,

$$\langle x\rangle = \frac{1}{N}\sum_{i=1}^{N} x_i, \tag{13}$$

and i is macro particle number. Here, x_c, y_c, β_{xc} and β_{yc} are

$$x_c = x - \langle x\rangle, \quad \beta_{xc} = \beta_x - \langle\beta_x\rangle, \tag{14}$$

$$y_c = x - \langle y\rangle, \quad \beta_{yc} = \beta_y - \langle\beta_y\rangle, \tag{15}$$

where $\beta_x = \dot{x}/c$, $\beta_y = \dot{y}/c$ and $\beta_z = \dot{z}/c$. Transverse normalized rms emittances are defined by

$$\epsilon_{nx} = \langle\gamma\rangle\sqrt{\langle x_c^2\rangle\langle\beta_{xc}^2\rangle - \langle x_c\beta_{xc}\rangle^2}, \tag{16}$$

$$\epsilon_{ny} = \langle\gamma\rangle\sqrt{\langle y_c^2\rangle\langle\beta_{yc}^2\rangle - \langle y_c\beta_{yc}\rangle^2}. \quad (17)$$

Longitudinal normalized rms emittance is defined by

$$\epsilon_{nz} = \frac{mc^2}{|q_e|}\sqrt{\langle t_c^2\rangle\cdot\langle\gamma_c^2\rangle - \langle t_c\gamma_c\rangle^2}, \quad (18)$$

where

$$t_c = t - \langle t\rangle, \quad (19)$$

$$\gamma_c = \gamma - \langle\gamma\rangle. \quad (20)$$

In order to calculate CS parameters in the merger section from GPT results, we enhanced routines which calculate CS parameters. The original routine is not convenient to calculate CS parameters in bending magnet. We added rotation of particle coordinates along beam trajectory to the routine. Using enhanced routine, we can calculate CS parameters in merger section. In order to check the enhanced routine and GPT input files, we calculated CS parameters for L0B1 merger and zigzag merger without space charge effect using `elegant` and GPT. The bending magnet in `elegant` have two parameters to control fringe field. They are 'HGAP' and 'FINT'. HGAP is half gap between magnetic poles, and FINT is field integral. In this case, we use HGAP = 25.0 mm and FINT = 0.5. In GPT, there are two parameters, b_1 and b_2 to control fringe field. The fringe field from entrance of magnet ($z = 0$) is given by [3]

$$B_y(z, y = 0) = \frac{1}{1 + \exp(b_1 z + b_2 z^2)}. \quad (21)$$

Using Eq. (8), we can translate fringe field parameters from `elegant` to GPT. In this case, we used $b_1 = 40.0$ and $b_2 = 0$ in the bending magnets.

Fig. 24 shows the calculated betatron functions for L0B1 merger using `elegant` and GPT. The betatron function calculated by GPT is almost same as the `elegant` results after the merger section. However, there is the difference of β_x in the merger section. It seems that the difference is caused by the difference of the emittance in the merger section as shown in Fig. 24 and Eq. (10). The calculated betatron functions for zigzag merger using `elegant` and GPT are shown in Fig. 25. Although there is the difference of β_x in the merger section, the betatron functions after the exit of merger are almost same as the `elegant` results. These results show that the input files for GPT can reproduce the linear optics. The input files for GPT were used in the optimization of beamline parameters.

2.3 Dispersion functions in particle tracking

In the merger section, coupling the dispersion function and longitudinal space charge force causes emittance growth. Before the study of the emittance growth, the dispersion function,

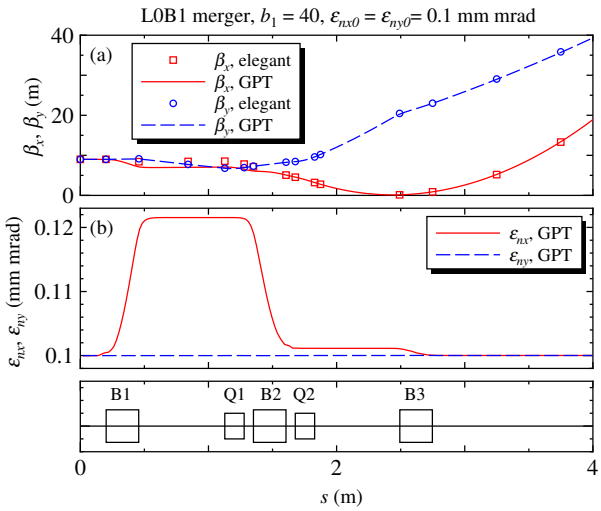

Figure 24: Betatron functions and emittances in L0B1 merger calculated by GPT and `elegant` without space charge effect. Initial twiss parameters are $\beta_x = \beta_y = 9.0$ m and $\alpha_x = \alpha_y = 0.0$.

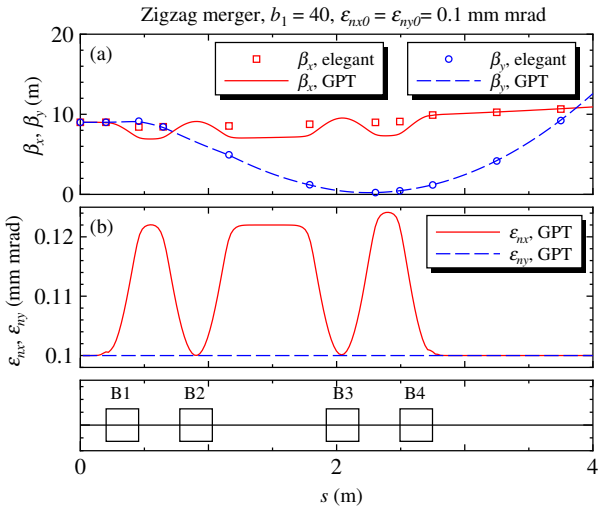

Figure 25: Betatron functions and emittances in zigzag merger calculated by GPT and `elegant` without space charge effect. Initial twiss parameters are $\beta_x = \beta_y = 9.0$ m and $\alpha_x = \alpha_y = 0.0$.

which calculated by GPT, are checked with out space charge effect to confirm the input files for GPT.

In this section, we define fourth different dispersion functions. η_{x0} is dispersion function which calculated by transfer matrix. It is the linear term of the dispersion function. In the particle tracking simulation, the linear term of dispersion can be calculated by two single particle tracking with different momentum without space charge effect,

$$\eta_{x1} = \frac{x_{p+\Delta p} - x_p}{\Delta p/p}. \tag{22}$$

Here, $x_{p+\Delta p}$ is orbit distortion for a single particle with momentum of $p + \Delta p$, and x_p is orbit distortion with momentum of p. In this case, the two trackings with a single particle are required to calculate η_{x1}. In usual particle tracking simulation, numerous particles are tracked, and the result is described by the distribution of six-dimensional phase space. Here, we define two new dispersion functions, which can be calculated by particle distribution. η_{x2} is defined by

$$\eta_{x2} = \frac{dx}{d(\Delta p/p)}, \tag{23}$$

in x-p space. η_{x2} corresponds to slope in x-p space distribution. η_{x3} is defined by

$$\eta_{x3} = \frac{\langle x(\Delta p/p)\rangle}{\langle(\Delta p/p)\rangle^2}. \tag{24}$$

The dispersion function is calculated from two rms values in x-p phase space. The calculations of η_{x2} and η_{x3} not required two trackings like as the calculation of η_{x1}.

Original GPT dose not have the routine to calculate dispersion function. To calculate dispersion function from GPT results, we developed new routine, 'dispx', 'dispy' and 'dispz'. The routine is based on the calculation of η_{x3}, Eq. (24). Figure 26 shows η_{x3} calculated by 'dispx' command from GPT result, and linear dispersion function, η_{x0}, calculated by `elegant` in the L0B1 merger with out space charge effect. The result of η_{x3} is same as the linear dispersion as shown in Fig. 26. Figure 27 shows η_{x3} calculated by 'dispx' command from GPT result, and linear dispersion function, η_{x0}, calculated by `elegant` in the zigzag merger with out space charge effect. The figures show that the result of Eq. (24) without space charge agrees with linear dispersion function. Thus, from the multi particle tracking results, we can calculate dispersion function using Eq. (24).

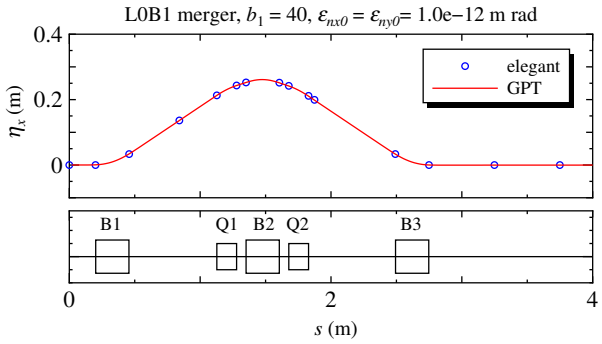

Figure 26: Linear dispersion function in L0B1 merger calculated by GPT and `elegant` without space charge effect.

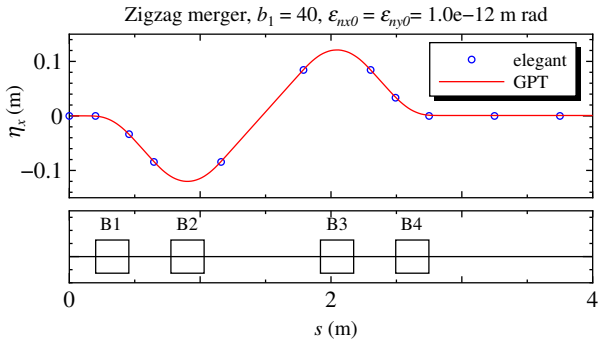

Figure 27: Linear dispersion function in zigzag merger calculated by GPT and `elegant` without space charge effect.

2.4 Decoupling condition for longitudinal space charge force

In this section, we show the decoupling condition in merger section. We consider that the energy deviation depends on s linearly, which is caused by longitudinal space charge (LSC) force. This case case is called "frozen case". Then, the energy deviation is given by

$$\delta(s) = \delta_0 + f(\zeta_0)s, \tag{25}$$

where ζ is the longitudinal deviation of a particle, which has time, $t(s)$, from the reference particle,

$$\zeta(s) = v_0(t_0(s) - t(s)), \tag{26}$$

$\zeta_0 = \zeta(s_0)$, and $f(\zeta_0)$ is a function of ζ_0. Here, v_0 and t_0 are the velocity and the time of the reference particle, respectively. For frozen case, the generalize dispersion becomes,

$$R(s) = \delta_0 R_1(s) + f(\zeta_0)R_2(s). \tag{27}$$

$R_s(s)$ is given by

$$R_2(s) = \begin{pmatrix} I_{1s}(s) \\ I_{2s}(s) \end{pmatrix}, \tag{28}$$

where

$$\begin{aligned} I_{1s}(s) &= \int_{s_0}^{s} s_1 K_o(s_1) m_{12}(s_1|s) ds_1 \\ &= m_{12}(s_0|s) I_{cs}(s) - m_{11}(s_0|s) I_{ss}(s), \end{aligned} \tag{29}$$

and

$$\begin{aligned} I_{2s}(s) &= \int_{s_0}^{s} s_1 K_o(s_1) m_{12}(s_1|s) ds_1 \\ &= m_{22}(s_0|s) I_{cs}(s) - m_{21}(s_0|s) I_{ss}(s). \end{aligned} \tag{30}$$

Here, $I_{cs}(s)$ and $I_{ss}(s)$ are defined by

$$I_{cs}(s) = \int_{s_0}^{s} s_1 K_o(s_1) m_{11}(s_0|s_1) ds_1, \tag{31}$$

$$I_{ss}(s) = \int_{s_0}^{s} s_1 K_o(s_1) m_{12}(s_0|s_1) ds_1. \tag{32}$$

The achromatic conditions for frozen case becomes

$$I_{1s}(s_f) = 0, \tag{33}$$

$$I_{2s}(s_f) = 0, \tag{34}$$

or using $I_{cs}(s)$ and $I_{ss}(s)$

$$I_{cs}(s_f) = 0, \tag{35}$$

$$I_{ss}(s_f) = 0. \tag{36}$$

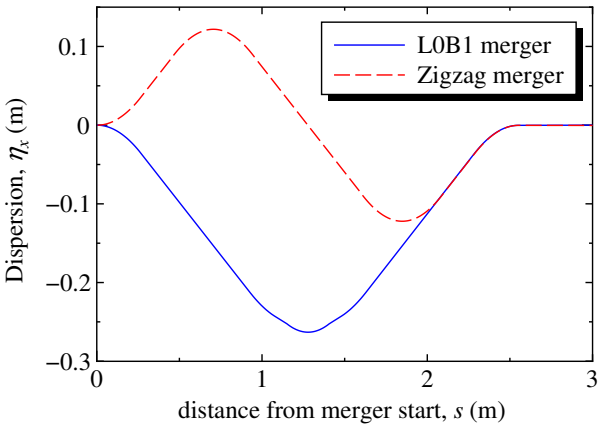

Figure 28: Dispersion functions in L0B1 and zigzag merger.

The zigzag merger is designed to satisfy the above nontrivial achromatic conditions. On the other hand, the L0B1 merger dose not satisfy the conditions.

The dispersion functions of the zigzag and L0B1 mergers are shown in Fig. 28. At the exit of merger s_f, the both mergers satisfy the normal achromatic conditions, $\eta_x(s_f) = 0$ and $\eta'_x(s_f) = 0$. The conditions are same as Eqs. (75) and (76) as shown in Appendix A. Calculated $I_c(s)$ and $I_s(s)$ are shown in Fig. 29. It shows that the both mergers satisfy the normal achromatic conditions. Figure 30 show the nontrivial achromatic conditions. The zigzag merger satisfies the conditions, Eqs .(35) and (36). On the other hand, the L0B1 merger have non zero values of $I_{cs}(s_f)$ and $I_{ss}(s_f)$. Therefore, in the L0B1 merger, the linear LSC dose not cancel, and the larger emittance growth compared with the zigzag merger is caused by it. In order to investigate the difference of the emittance growth, we carried out the optimization of the beamline parameters for both of the mergers.

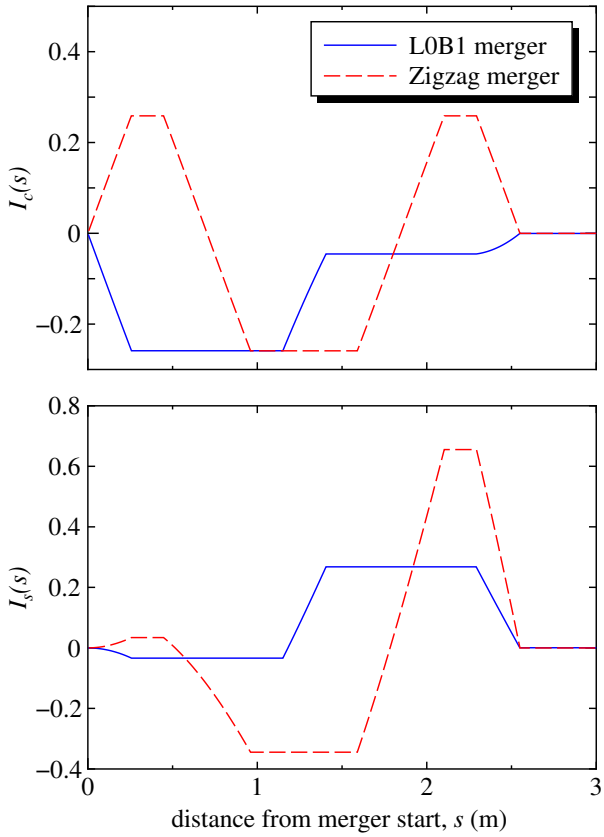

Figure 29: Optics functions, $I_c(s)$ and $I_s(s)$. Dispersion functions, η_x, is given by $\eta_x = I_c(s) - I_s(s)$.

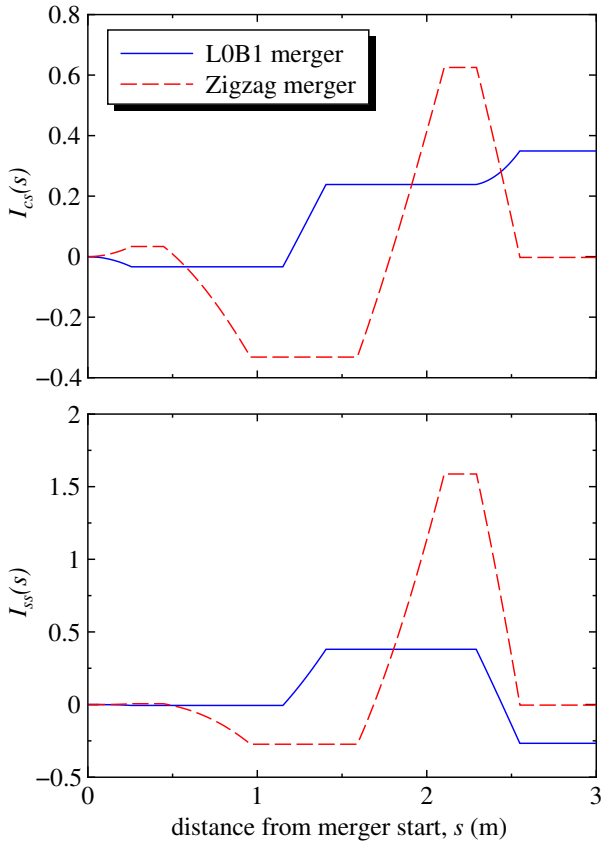

Figure 30: Optics functions, $I_{cs}(s)$ and $I_{ss}(s)$.

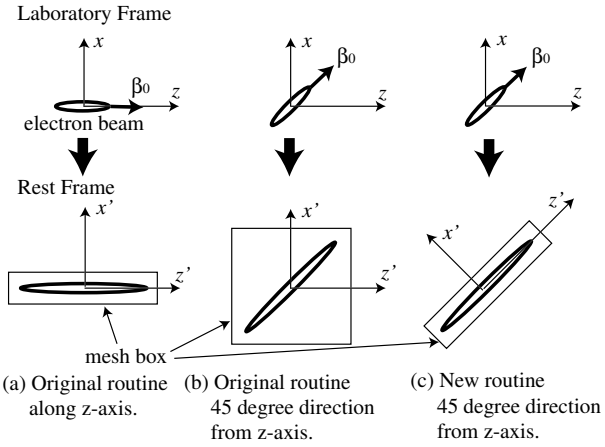

Figure 31: Bounding box sizes in the rest frame for the original GPT space charge mesh routine and enhanced space charge routine.

2.5 Space charge calculation in merger section by GPT

In GPT 3D space charge mesh routine, the particle coordinates are transferred from the laboratory frame to the rest frame to calculate space charge field according to $\boldsymbol{r}'_{\perp} = \boldsymbol{r}_{\perp}$ and $\boldsymbol{r}'_{\parallel} = \gamma \boldsymbol{r}_{\parallel}$ as shown Fig. 31. Here, $\boldsymbol{r}_{\perp}$ is the transverse coordinate, and $\boldsymbol{r}_{\parallel}$ is the longitudinal coordinate. When the bunch does not move along z-axis, the bounding box ends up improperly oriented as illustrated in Fig. 31-(a) and (b). In this case, for example, the transverse emittance incorrectly depends on the angle of orbit for a straight trajectory to z-axis. In order to check the effect, the particle tracking simulations were carried in the drift spaces with different angle from z-axis. The particle orbits are shown in Fig. 32. In this case, the emittance must not depend on the angle from z-axis. However, for the original space charge routine, the time evolutions of the emittance and the energy spread depend on the angle from z-axis as shown in Figs. 33-(a) and 34-(a), respectively. To fix this problem, we have added a transformation of rotation in the rest frame in the space charge routine. Using the enhanced space charge routine, we are able to calculate transverse emittance and energy spread accurately for an orbit with a finite angle to z-axis as shown in Fig. 33-(b) and 34. In this study, the enhanced routine was used instead of the original routine.

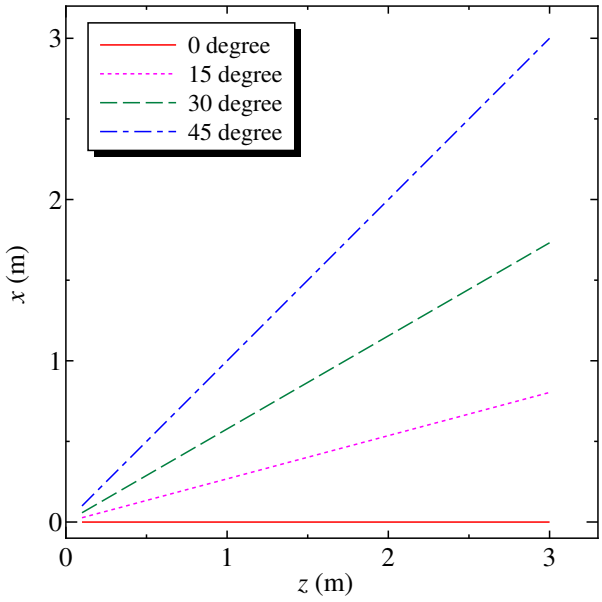

Figure 32: Reference orbit to check space charge routines in GPT. The particles move on straight lines with different angles from z-axis.

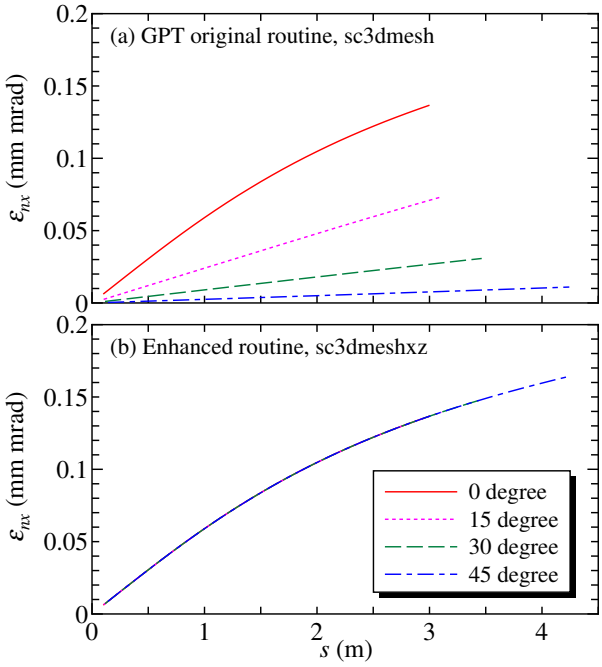

Figure 33: Normalized rms emittances calculated by original and enhanced routines. The particles moves on orbits, which are shown in Fig. 32.

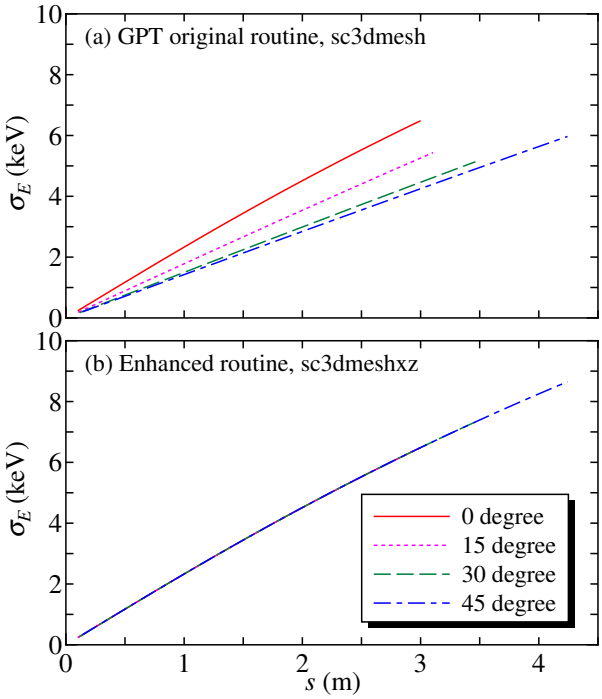

Figure 34: Energy spread calculated by original and enhanced routines. The particles moves on orbits, which are shown in Fig. 32.

2.6 Optimization of merger section

In order to study emittance growth in merger section, optimizations of beamline parameters were carried out using GPT. The emittance growth in three types of mergers, L0B1 merger, zigzag merger and pure drift, were estimated. In the optimization, two beam parameters were minimized by multi-objective method. They are transverse emittance and rms bunch length or kinetic energy at the exit of the beamline. Since the beam dose not have cylindrical symmetry after exit of merger section, the horizontal emittance is not same as the vertical emittance. Therefore, both the horizontal and vertical emittance must be minimized to obtain minimum transverse emittance. In order to minimize both the emittances, we defined the following two values as objectives in the optimization. One is the maximum of ϵ_{nx} and ϵ_{ny}, $\max(\epsilon_{nx}, \epsilon_{ny})$ and the other one is $\mathrm{sqrt}(\epsilon_{nx} \cdot \epsilon_{ny})$. For minimizing $\max(\epsilon_{nx}, \epsilon_{ny})$,

$$\max(\epsilon_{nx}, \epsilon_{ny}) \geq \epsilon_{nx} \text{ and } \epsilon_{ny}, \tag{37}$$

and ϵ_{nx} or ϵ_{ny} is equal to $\max(\epsilon_{nx}, \epsilon_{ny})$. In this case, difference between ϵ_{nx} and ϵ_{ny} dose not become larger. On the other hand, for minimizing $\mathrm{sqrt}(\epsilon_{nx} \cdot \epsilon_{ny})$,

$$\sqrt{\epsilon_{nx} \cdot \epsilon_{ny}} \geq \epsilon_{nx} \text{ or } \epsilon_{ny}, \tag{38}$$

and both ϵ_{nx} and ϵ_{ny} may not decrease. In optimization, three optimizations with the following combinations of objectives were carried out. They are minimizing $\max(\epsilon_{nx}, \epsilon_{eny})$ and σ_z, minimizing $\mathrm{sqrt}(\epsilon_{nx} \cdot \epsilon_{ny})$ and σ_z, and minimizing $\max(\epsilon_{nx}, \epsilon_{ny})$, $\mathrm{sqrt}(\epsilon_{nx} \cdot \epsilon_{ny})$ and E_0.

The beam has uniform elliptical distribution in x-y plane, and uniform distribution for longitudinal direction. The elliptical distribution is described by initial rms beam sizes, σ_{x0} and σ_{y0}. The initial bunch length, σ_{z0}, distinguishes the longitudinal distribution. In order to study emittance growth in merger section, initial horizontal and vertical emittances are zero. However, to reproduce effect of $\alpha_{x,cs}$ and $\alpha_{y,cs}$, distribution in transverse velocity space is set as the following. The distribution in x-β_x phase space is tilted by a parameter, d_x. The tilted distribution is given by

$$\gamma\beta_x = \gamma\beta_{x0} + d_x \left(x - \langle x \rangle\right), \tag{39}$$

$$\gamma\beta_z = \sqrt{\gamma^2 - \gamma^2\beta_x^2 - \gamma\beta_y^2 - 1}, \tag{40}$$

where β_{x0} is v_{x0}/c before tilting the distribution. Similarly, the distribution in y-β_y phase space is tilted by

$$\gamma\beta_y = \gamma\beta_{y0} + d_y \left(y - \langle y \rangle\right), \tag{41}$$

$$\gamma\beta_z = \sqrt{\gamma^2 - \gamma^2\beta_x^2 - \gamma\beta_y^2 - 1}. \tag{42}$$

Since we set the distribution as $\beta_{x0} = \beta_{y0} = 0$, the velocity distribution after tilting becomes

$$\beta_x = \frac{d_x}{\gamma} x_c, \tag{43}$$

$$\beta_y = \frac{d_y}{\gamma} y_c. \tag{44}$$

In this case, the transverse emittances calculated by Eq. (16) and (17) are zero. If the initial horizontal and vertical emittances are not zero, $\alpha_{x,cs}$ and $\alpha_{y,cs}$ can be described by

$$\alpha_{x,cs} = -\frac{d_x \sigma_x^2}{\epsilon_{nx}}, \tag{45}$$

$$\alpha_{y,cs} = -\frac{d_y \sigma_y^2}{\epsilon_{ny}}. \tag{46}$$

Thus, the parameters, d_x and d_y, correspond to $\alpha_{x,cs}$ and $\alpha_{y,cs}$ with zero transverse emittances. The longitudinal velocity distribution is uniform distribution. The initial kinetic energy E_0 distinguishes it. E_0 for minimizing emittances and bunch length, is 10 MeV. For minimizing emittances and initial kinetic energy, it is varied in the optimization.

In the optimization, we used the above fourth beamlines, L0B1 with fixed quadrupole strengths, L0B1 with varied quadrupole strength, zigzag merger, and pure drift as shown in Fig. 22. The L0B1 merger has two quadrupole magnet to adjust achromatic condition. In the optimization of L0B1 with fixed Qs, the quadrupole strengths, $K_{1,Q1}$ and $K_{1,Q2}$, are fixed to satisfies achromatic condition at the exit of merger. In the optimization of L0B1 with varied Qs, $K_{1,Q1}$ and $K_{1,Q2}$ are varied in the optimization to minimize objectives. In this case, the achromatic condition for linear optics is not satisfied, but varying quadrupole strengths may decrease transverse emittance at the end of beamline by space charge effect. To investigate it, we added the optimization for L0B1 with varied Qs.

Table 13 shows variables in the optimizations for four types of beamlines. Here, K_1 is quadrupole magnetic field strength, and $E_{CTE01-5}$ are maximum electric fields in main SRF cavities. The phases of the main SRF cavities were optimized to give maximum acceleration. Courant-Snyder parameters at end of beamline were restricted to connect beam optics to first arc section in a return loop section in ERL. The constraints in the optimizations are shown in Table 14.

The optimization was carried with the following three steps. In the first step, the optimization with 2 k particles and Alpha of 1.0 was carried. Initial beamline parameters were random. The number of generations was 100 - 200 generations. The simulation time with 100 generation was about 16 hours. In the second step, the optimization with 2 k particles and Alpha of 2.5 was carried. As initial parameters, the results of the first step was used. The number of generations is 50-100 generations. In the final step, the optimization with 30 k particles was carried using the results of 2 k particles with Alpha of 2.5 as initial parameters. The number of generations was 30.

In the calculations, non-equidistance mesh based space charge routine was used. Number of macro particles is 2 k particles or 30 k particles. As a space charge routine, the enhanced space charge routine was used. Initial transverse distribution is uniform elliptical distribution,

variable	L0B1 with fixed Q	L0B1 with varied Q	zigzag	drift
σ_{x0} (mm)	0.01-0.2	0.001-0.5	0.01-1.0	0.005-1.5
σ_{y0} (mm)	0.5-1.8	0.1-1.8	0.005-1.0	same as σ_{x0}
d_x (rad/m)	-30-30	-40-10	-30.0-0.0	-30-10
d_y (rad/m)	-20-10	-20-10	-35.0-20.0	same as d_x
σ_{z0} (mm)	0.4-1.0	0.4-1.0	0.4-1.0	0.4-1.0
$K_{1,QUB01}$ (m^{-2})	3.939	3.5-5.5	-	-
$K_{1,QUB02}$ (m^{-2})	3.939	4.0-6.0	-	-
E_{CTE01} (MV/m)	5-30	5-30	5-30	5-30
E_{CTE02} (MV/m)	5-30	5-30	5-30	5-30
$E_{CTE03-5}$ (MV/m)	30	30	30	30

Table 13: Variables in optimization.

constraint	range
$\alpha_{x,cs}$	> 0
$\alpha_{y,cs}$	> 0
$\beta_{x,cs}$	< 100 (m)
$\beta_{y,cs}$	< 100 (m)

Table 14: Constraints at exit of beamline in optimization.

and initial longitudinal distribution is uniform distribution. Initial transverse emittances were zero. Initial energy spread was 0.001. Space charge parameters for 2k particles were Alpha=2.5, Fn=0.5, Nstd=5, macc=0.6, Gbacc=5.5, and xacc=6.5. Space charge parameters for 30k particles were Alpha=2.0, Fn=0.5, Nstd=5, macc=0.3, Gbacc=5.0, and xacc=8.0.

The optimizations were carried with the above conditions and 80 pC bunch charge. In next subsection, optimization results are described.

2.7 Optimization results for merger section

2.7.1 Minimize max($\epsilon_{nx}, \epsilon_{ny}$) and σ_z

In the simulations, initial kinetic energy and bunch charge were fixed to be 10 MeV and 80 pC, respectively. Optimization results to minimize $\max(\epsilon_{nx}, \epsilon_{ny})$ and σ_z are shown in Figure 35. Emittance growth in pure drift beamline is estimated to be less than 0.1 mm mrad. It indicates that the emittance growth caused by space charge effect alone is less than 0.1 mm mrad. In the other beamline, the emittance growth caused by space charge effect and dispersion function is added to it. The results in the zigzag merger are less than the results in the L0B1 merger. It shows that the nontrivial achromatic condition for longitudinal linear space charge is effective to reduce emittance growth in merger section. For L0B1 mergers, the results with varied quadrupole strengths are less than the results with fixed quadrupole strengths. Therefore, to tune quadrupole strengths are effective to reduce emittance growth caused in merger section. Figure 36 shows the horizontal and vertical emittances. The horizontal emittance is larger than the vertical emittance for every case. Figure 37 shows the horizontal and vertical rms beam size at the end of beamline, and Figure 38 shows the kinetic energy and the rms energy spread. The results for L0B1 mergers have lower kinetic energy compared with one for zigzag and pure drift. It is caused by lower accelerating electric fields in SRF1 and SRF2 as shown in Figure 43. The rms energy spread is less than 36 keV as shown in Figure 38. The Courant-Snyder parameters are shown in Figure 39 and 40. Both α_{cs} and β_{cs} satisfy the constraint conditions, Table 14.

Optimized initial rms beam sizes and slopes in x-β_x and y-β_y spaces are shown in Figure 41 and 42, respectively. Figure 43 shows optimized initial rms bunch length, and electric field strengths of first and second SRF cavities. L0B1 merger chose minimum electric field of 5 MV/m as shown Figure 43, and it caused the lower kinetic energy at the end of beamline as shown in Figure 38.

Time evolutions of beam parameters with 0.8 mm bunch length at the end of beamline were calculated. Table 15 shows the optimized beamline parameters. Time evolutions of normalized rms emittances are shown in Figure 44. For pure drift, emittance growth is caused before main SRF section. Since the beam energy is 10 MeV before the main SRF section, the space charge effect is still effective, and caused emittance growth. After the main SRF section, emittance is kept almost same value. The zigzag merger, which has nontrivial achromatic condition, has next smallest emittance. The simulation results shows that nontrivial achromatic condition for longitudinal space charge is effective to reduce emittance growth in merger section. For L0B1 mergers, we can reduce emittance growth to vary quadrupole strengths in merger section, Figure 45 shows time evolutions of rms beam sizes and bunch length with optimized beamline parameters. For L0B1 and zigzag mergers, the bunch length is elongated by dispersion function in the merger section. On the other hand, the bunch length for pure drift is kept almost same. Figure 45 shows time evolutions of rms beam sizes and bunch length with optimized beamline parameters. The energy difference is caused by the difference of accelerating electric fields for SRF1 and SRF2 cavities. The accelerating electric field strength of main SRF cavity affects

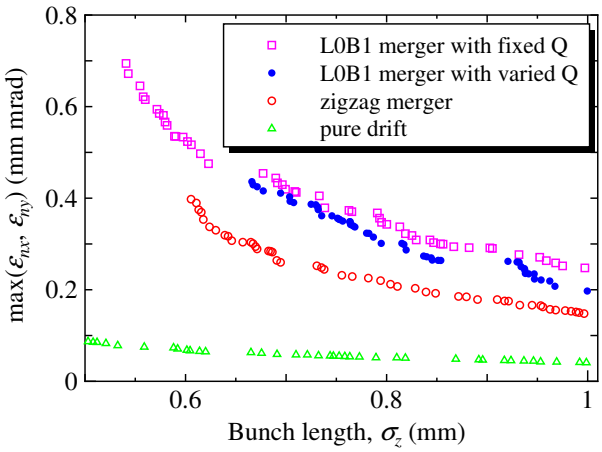

Figure 35: Optimization results to minimize $\max(\epsilon_{nx}, \epsilon_{ny})$ and σ_z. The horizontal and vertical axes are $\max(\epsilon_{nx}, \epsilon_{ny})$ and σ_z, respectively.

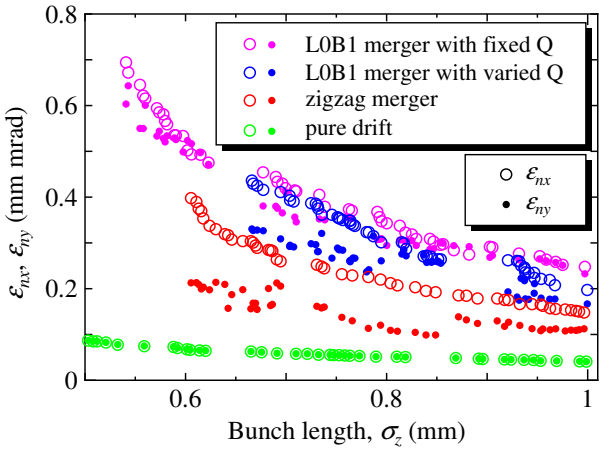

Figure 36: Horizontal and vertical normalized rms emittances at end of beamline. The horizontal axis is same as Fig. 35.

focusing for transverse beam size. To satisfy the constraint condition as shown in Table 14, lower field strengths are chosen for L0B1 merger with fixed quadrupole strengths. It shows that Figure 47 and 48. To tune the Courant-Snyder parameters without varying electric field strengths of main SRF cavity, adding quadrupole magnets between main SRF cavities may be effective. Table 16 shows optimized beam parameters with $\sigma_z = 0.8$ mm at end of beamline. The emittances at the end of beamline for L0B1 with fixed quadrupoles, L0B1 with varied quadrupoles, zigzag and pure drift are 0.338, 0.297, 0.231 and 0.052 mm mrad, respectively. The results shows that the zigzag merger has advantage to reduce emittance growth. However, to adjust the quadrupole strengths in merger section, the emittance growth for L0B1 merger can approach one for zigzag merger. In addition, L0B1 merger has advantage for layout of beamline. Therefore, L0B1 merger is better than other types of merger for Cornell University ERL.

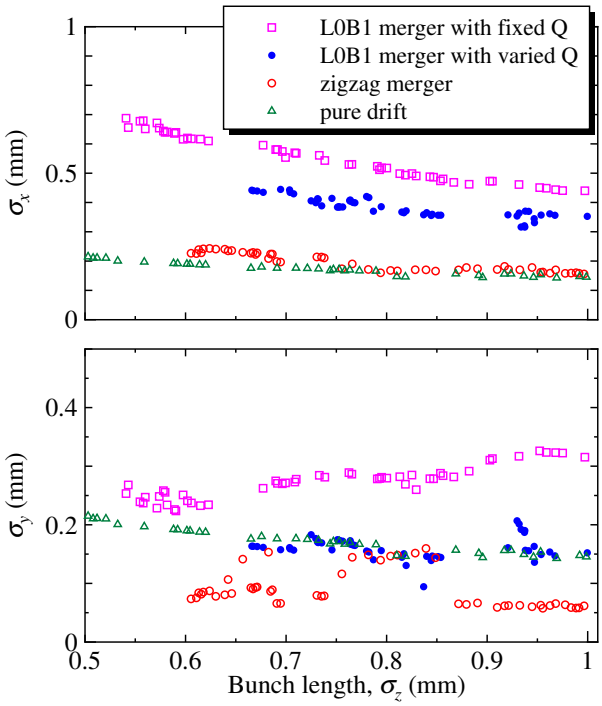

Figure 37: Horizontal and vertical rms beam size at end of beamline. The horizontal axis is same as Fig. 35.

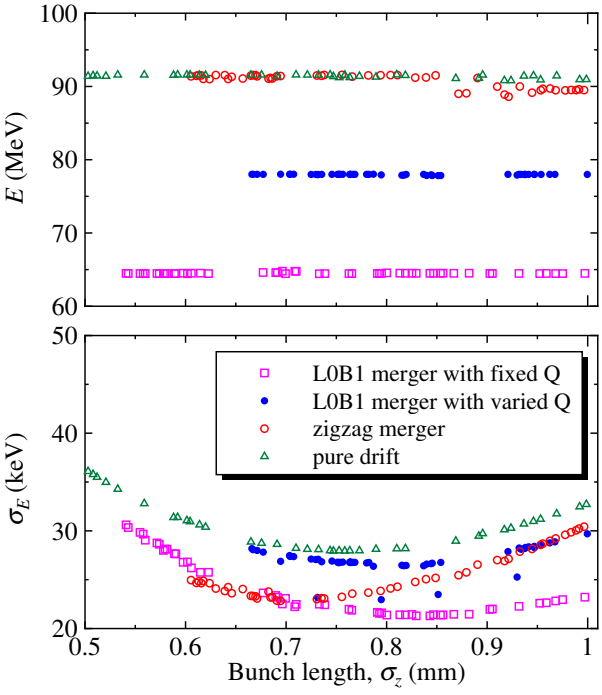

Figure 38: Kinetic energy and rms energy spread at end of beamline. The horizontal axis is same as Fig. 35.

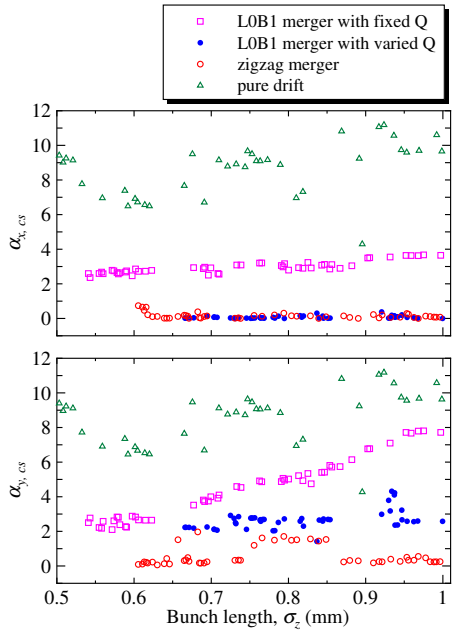

Figure 39: $\alpha_{x,cs}$ and $\alpha_{y,cs}$ of Courant-Snyder parameters at end of beamline. The horizontal axis is same as Fig. 35.

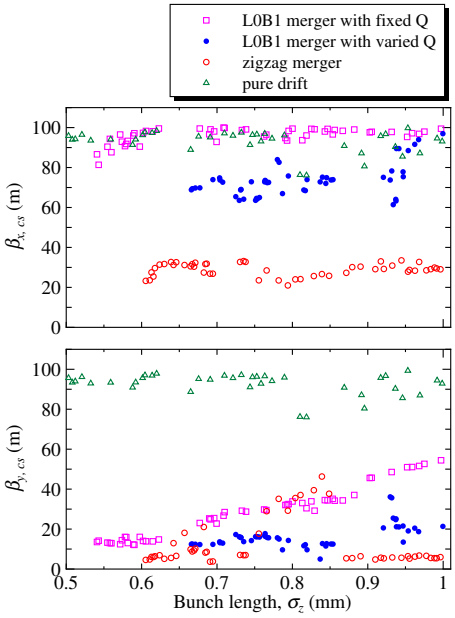

Figure 40: $\beta_{x,cs}$ and $\beta_{y,cs}$ of Courant-Snyder parameters at end of beamline. The horizontal axis is same as Fig. 35.

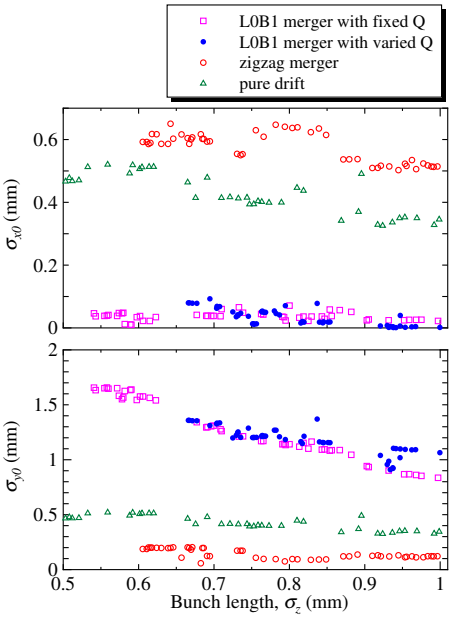

Figure 41: Optimized initial rms beam sizes at entrance of beamline. The horizontal axis is same as Fig. 35.

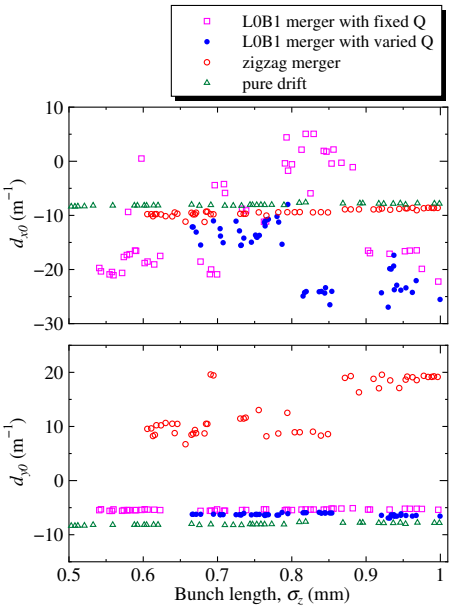

Figure 42: Optimized initial slopes, d_x and d_y, in x-β_x and y-β_y phase spaces, respectively. The horizontal axis is same as Fig. 35.

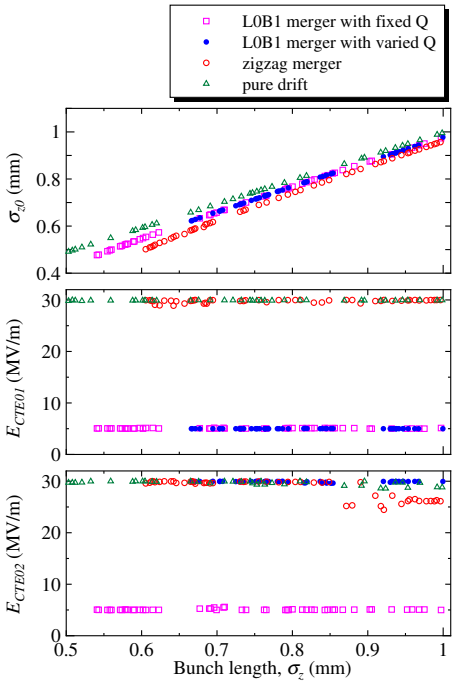

Figure 43: Optimized initial rms bunch length, and electric field strengths of first and second SRF cavities. The horizontal axis is same as Fig. 35.

variable	L0B1 with fixed Q	L0B1 with varied Q	zigzag	drift
σ_{x0} (mm)	0.071088	0.0708191	0.0637024	0.044646
σ_{y0} (mm)	1.14131	1.18388	0.0963629	same as σ_{x0}
d_x (rad/m)	−0.562789	−7.97395	−9.40809	−7.66885
d_y (rad/m)	−5.44686	−6.10295	8.92853	same as d_x
σ_{z0} (mm)	0.767556	0.762532	0.745559	0.805005
$K_{1,QUB01}$ (m^{-2})	3.939	3.58272	-	-
$K_{1,QUB02}$ (m^{-2})	3.939	5.15707	-	-
E_{CTE01} (MV/m)	5.12301	5.00119	29.9825	29.9489
E_{CTE02} (MV/m)	5.13202	29.8304	29.8736	29.9836
$E_{CTE03-5}$ (MV/m)	30	30	30	30

Table 15: Optimized beamline parameters with $\sigma_z = 0.8$ mm at end of beamline.

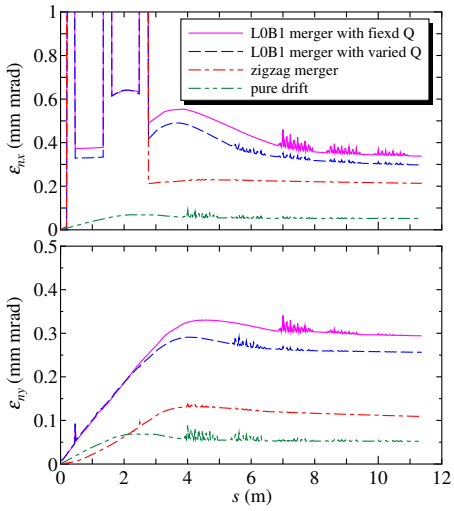

Figure 44: Time evolutions of normalized rms emittances in L0B1 beamline with varied quadrupole magnets. The optimized beamline parameters with the bunch length of 0.8 mm at the end of beamline are shown in Table 15.

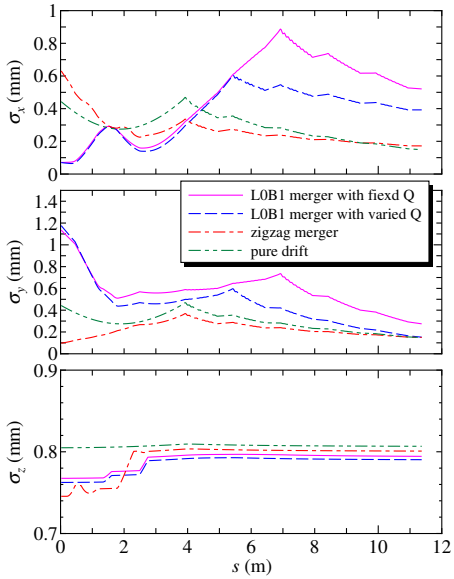

Figure 45: Time evolutions of rms beam sizes and bunch length with optimized beamline parameters. The bunch length at the end of beamline is 0.8 mm.

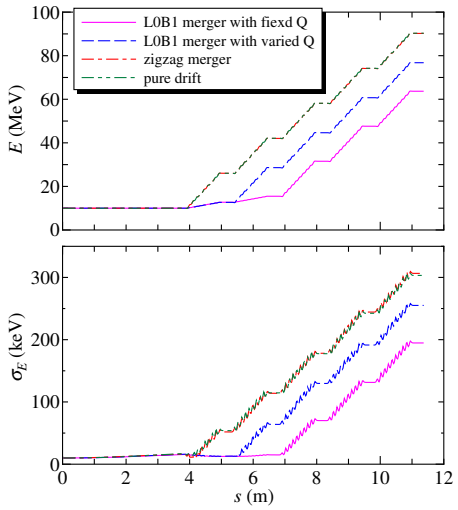

Figure 46: Time evolutions of kinetic energy and rms energy spread with optimized beamline parameters. The bunch length at the end of beamline is 0.8 mm.

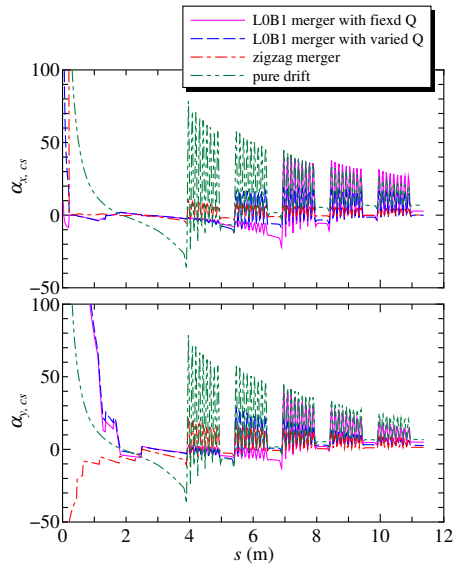

Figure 47: Time evolutions of $\alpha_{x,cs}$ and $\alpha_{y,cs}$ with optimized beamline parameters. The bunch length at the end of beamline is 0.8 mm.

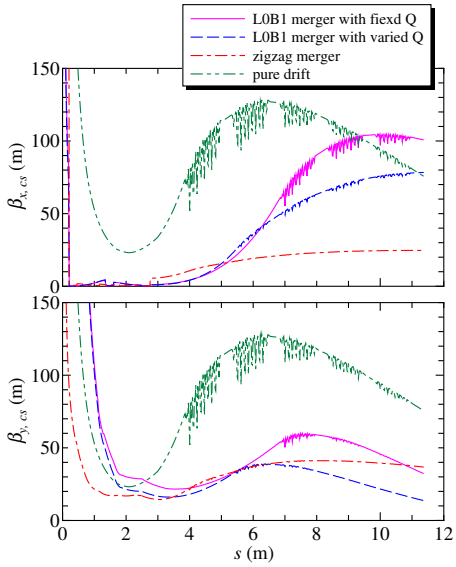

Figure 48: Time evolutions of $\beta_{x,cs}$ and $\beta_{y,cs}$ with optimized beamline parameters. The bunch length at the end of beamline is 0.8 mm.

variable	L0B1 with fixed Q	L0B1 with varied Q	zigzag	drift
ϵ_{nx} (mm mrad)	0.338	0.297	0.213	0.0520
ϵ_{ny} (mm mrad)	0.294	0.256	0.109	0.0522
ϵ_{nz} (eV s)	4.754×10^{-8}	5.234×10^{-8}	5.914×10^{-8}	6.385×10^{-8}
σ_x (mm)	0.521	0.392	0.172	0.149
σ_y (mm)	0.275	0.152	0.150	0.149
σ_z (mm)	0.794	0.790	0.801	0.807
E (MeV)	63.689	76.771	90.222	90.331
σ_E (keV)	194.754	255.044	306.537	303.273
$\alpha_{x,cs}$	2.791	−0.0321	0.101	6.696
$\alpha_{y,cs}$	4.861	2.650	1.411	6.675
$\beta_{x,cs}$ (m)	100.780	78.403	24.676	75.703
$\beta_{y,cs}$ (m)	3.227	13.693	36.752	75.581

Table 16: Optimized beam parameters with $\sigma_z = 0.8$ mm at end of beamline. The values were calculated with optimized beamline parameters as shown in Table 15.

2.7.2 Minimize sqrt($\epsilon_{nx}\epsilon_{ny}$) and σ_z

In the simulations, initial kinetic enegy and bunch charge were fixed to be 10 MeV and 80 pC, respectively. Optimization to minimize sqrt($\epsilon_{nx}\epsilon_{ny}$) and σ_z is carried out for L0B1 merger with varied quadrupole strengths. Optimization results to minimize sqrt($\epsilon_{nx}\epsilon_{ny}$) and σ_z are shown in Figure 49. Minimizing max(ϵ_{nx}, ϵ_{ny}) gives smaller emittance compared with minimizing sqrt($\epsilon_{nx}\epsilon_{ny}$). However, the difference is not so large. Figure 50 shows the horizontal and vertical rms beam size at end of beamline. For minimizing max(ϵ_{nx}, ϵ_{ny}), the horizontal emittance is almost same as the vertical emittance. On the other hand, the difference between the horizontal and vertical emittances for minimizing sqrt($\epsilon_{nx}\epsilon_{ny}$) is larger than one for minimizing max(ϵ_{nx}, ϵ_{ny}). In this case, the vertical emittance is extremely small, and almost same as the results for pure drift beamline as shown in Figure 36. However, the horizontal emittance is extremely large, and is distributed from 0.6 to 2.5 mm mrad. Since the product of ϵ_{nx} and ϵ_{ny} is minimized in this case, sqrt($\epsilon_{nx}\epsilon_{ny}$) with smaller ϵ_{ny} becomes smaller, if ϵ_{nx} has larger value. In actual beam operation, it is required that the both horizontal and vertical emittances are smaller. Therefore, minimizing max(ϵ_{nx}, ϵ_{ny}) is better to optimize beamline parameters.

Figure 51 shows the horizontal and vertical rms beam size at the end of beamline. The horizontal beam sizes for minimizing sqrt($\epsilon_{nx}\epsilon_{ny}$) is smaller than one for minimizing max(ϵ_{nx}, ϵ_{ny}). Thus, it seems that larger horizontal emittance growth for minimizing sqrt($\epsilon_{nx}\epsilon_{ny}$) is caused by larger size of horizontal momentum spread, σ_{β_x}. Kinetic energy and rms energy spread at end of beamline are shown in Figure 52. Figures 53 and 54 show Courant-Snyder parameters at end of beamline. The results of the Courant-Snyder parameters satisfy the constraint condition as shown in Table 14.

The results shows that to minimize both horizontal and vertical emittances, minimizing max(ϵ_{nx}, ϵ_{ny}) is better than minimizing sqrt($\epsilon_{nx}\epsilon_{ny}$).

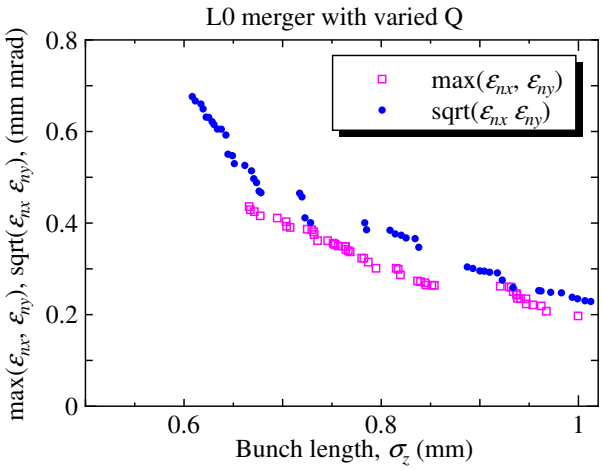

Figure 49: Optimization results to minimize sqrt($\epsilon_{nx}\epsilon_{ny}$) and σ_z. The horizontal axis is max($\epsilon_{nx}, \epsilon_{ny}$) or sqrt($\epsilon_{nx}\epsilon_{ny}$). The vertical axis is kinetic energy, E.

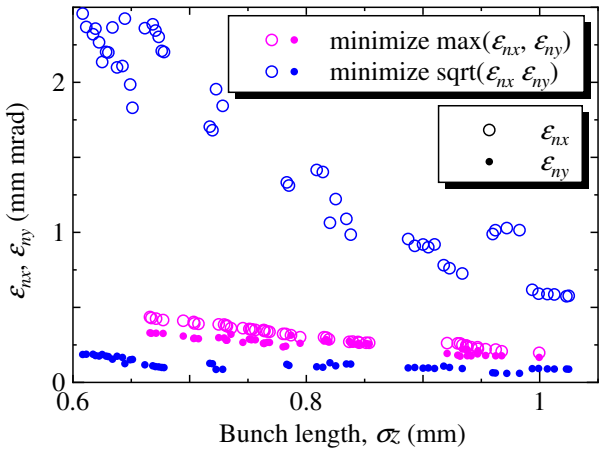

Figure 50: Horizontal and vertical rms beam size at end of beamline. The horizontal axis is same as Fig. 49.

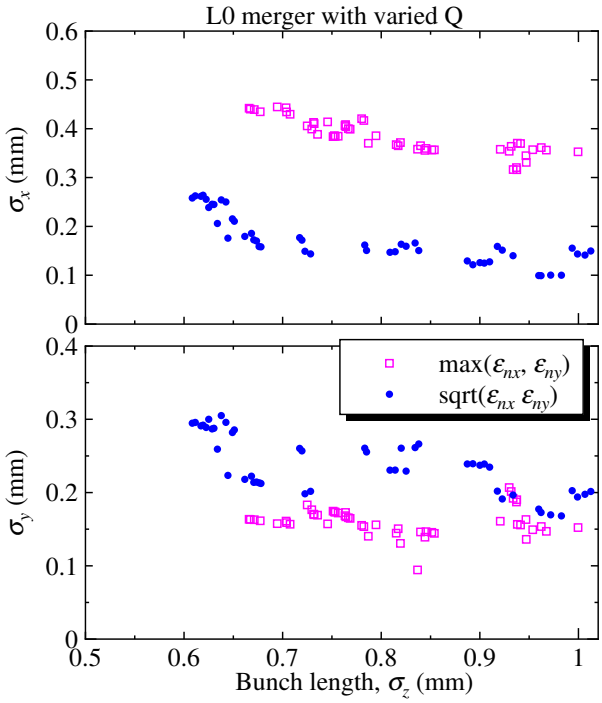

Figure 51: Horizontal and vertical rms beam size at end of beamline. The horizontal axis is same as Fig. 49.

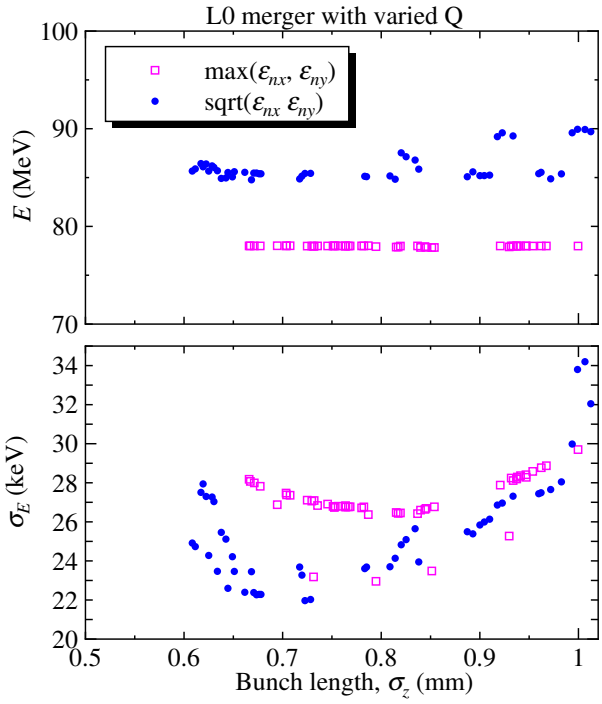

Figure 52: Kinetic energy and rms energy spread at end of beamline. The horizontal axis is same as Fig. 49.

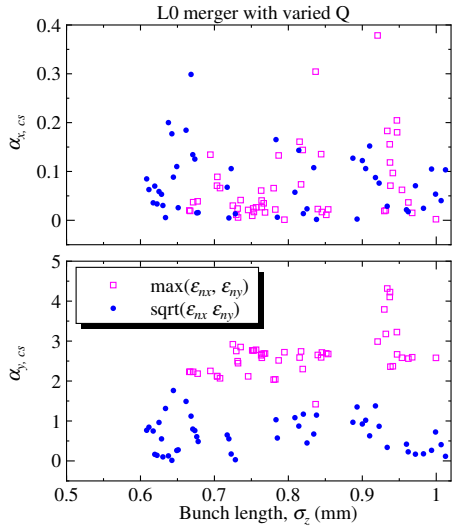

Figure 53: $\alpha_{x,cs}$ and $\alpha_{y,cs}$ of Courant-Snyder parameters at end of beamline. The horizontal axis is same as Fig. 49.

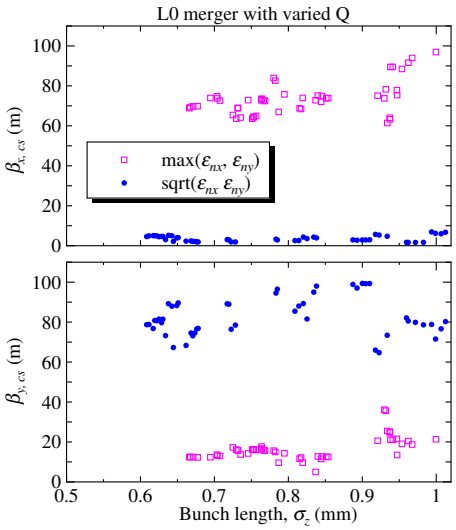

Figure 54: $\beta_{x,cs}$ and $\beta_{y,cs}$ of Courant-Snyder parameters at end of beamline. The horizontal axis is same as Fig. 49.

2.7.3 Minimize emittance and initial kinetic energy

In order to study effect of initial kinetic energy, optimizations to minimize max(ϵ_{nx}, ϵ_{ny}) or sqrt($\epsilon_{nx}\epsilon_{ny}$) and initial kinetic energy were carried out for L0B1 merger with varied quadrupole strengths. In the simulations, initial bunch length and bunch charge were fixed to be 0.9 mm and 80 pC, respectively. Figure 55 shows optimization results to minimize max($\epsilon_{nx}, \epsilon_{ny}$) or sqrt($\epsilon_{nx}\epsilon_{ny}$), and initial kinetic energy, E. Although, minimizing max(ϵ_{nx}, ϵ_{ny}) gives smaller emittance compared with minimizing sqrt($\epsilon_{nx}\epsilon_{ny}$) for lower initial kinetic energy, dependences of emittance on initial kinetic energy for both optimizations for high initial energy are almost same. Since space charge effect becomes weaker for higher initial energy, the emittance growth decreases depended on initial energy. For 20 MeV initial kinetic energy, the emittance growth is less than 0.05 mm mrad. The results show that the higher initial energy have advantage to reduce emittance growth. Figure 56 shows horizontal and vertical rms normalized emittances at end of beamline. When the initial kinetic energy is grater than 12 MeV, the horizontal emittance become almost same as the vertical emittance for both optimizations. Horizontal and vertical rms beam size at end of beamline are shown in Figure 57. The horizontal beam sizes are less than 0.5 mm, ant the vertical beam sizes are less than 0.7 mm at the end of beamline. Figure 58 shows kinetic energy and rms energy spread at end of beamline. The kinetic energies at the end of beamline are distributed from 72 to 93 MeV. The rms energy spreads are less than 30 keV. Figures 59 and 60 show Courant-Snyder parameters at end of beamline. In the optimization, constraint conditions for Courant-Snyder parameters were relaxed to be less than 500 m, to obtain the optimization results. The case of higher initial energy chose higher horizontal betatron function as shown in Figure 60. To avoid the higher betatron functions, it seems that adding quadrupole magnets between SRF cavities is effective.

The results of the optimization to minimize emittance and initial kinetic energy shows that the initial kinetic energy before the merger section is very important to reduce the emittance growth in the merger section.

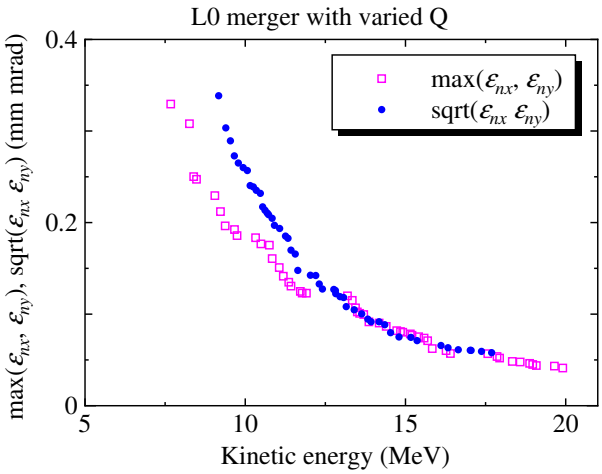

Figure 55: Optimization results to minimize $\max(\epsilon_{nx}, \epsilon_{ny})$‘ or $\mathrm{sqrt}(\epsilon_{nx}\epsilon_{ny})$, and initial kinetic energy, E. The horizontal axis is $\max(\epsilon_{nx}, \epsilon_{ny})$ or $\mathrm{sqrt}(\epsilon_{nx}\epsilon_{ny})$. The vertical axis is kinetic energy, E.

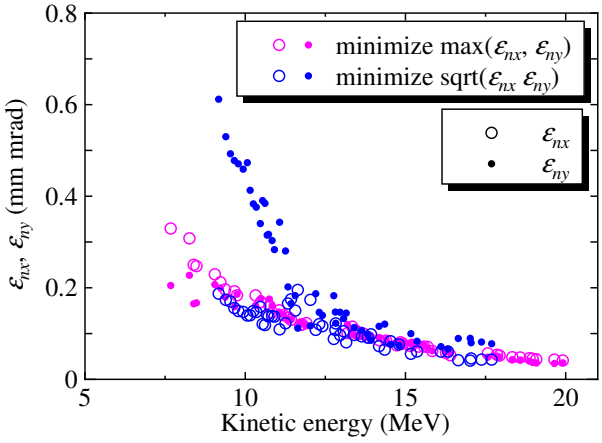

Figure 56: Horizontal and vertical rms normalized emittances at end of beamline. The horizontal axis is same as Fig. 55.

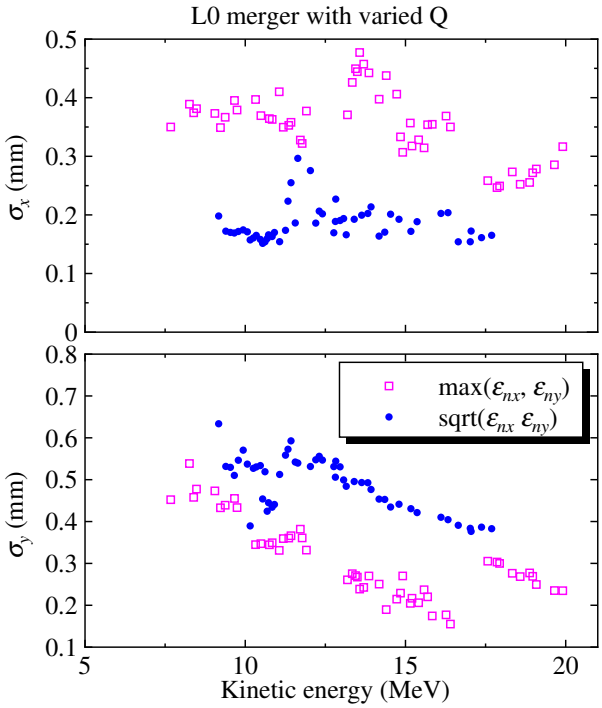

Figure 57: Horizontal and vertical rms beam size at end of beamline. The horizontal axis is same as Fig. 55.

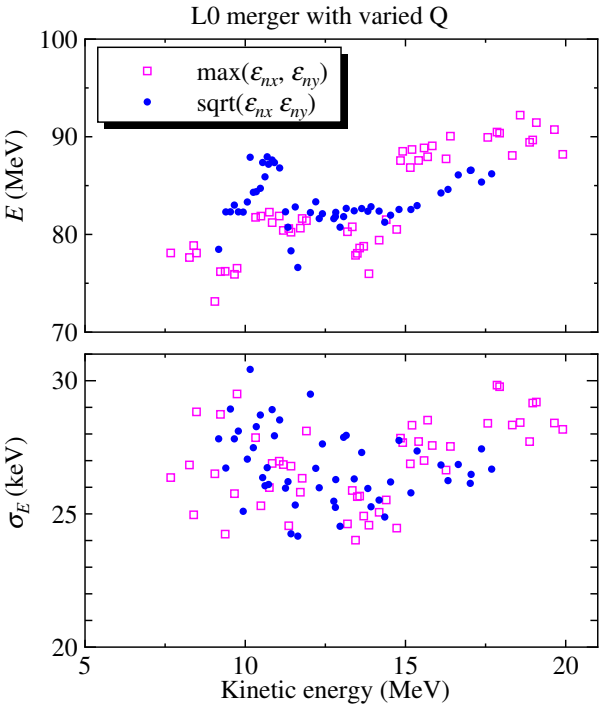

Figure 58: Kinetic energy and rms energy spread at end of beamline. The horizontal axis is same as Fig. 55.

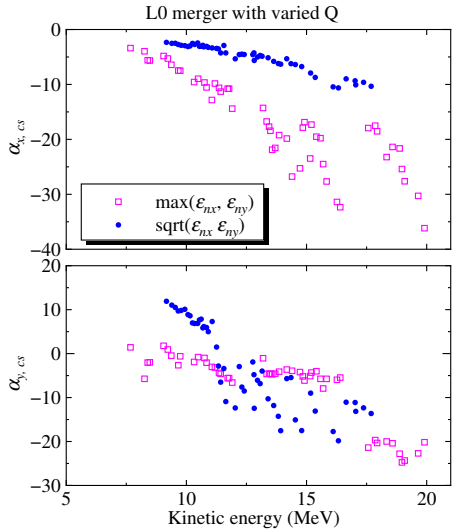

Figure 59: $\alpha_{x,cs}$ and $\alpha_{y,cs}$ of Courant-Snyder parameters at end of beamline. The horizontal axis is same as Fig. 55.

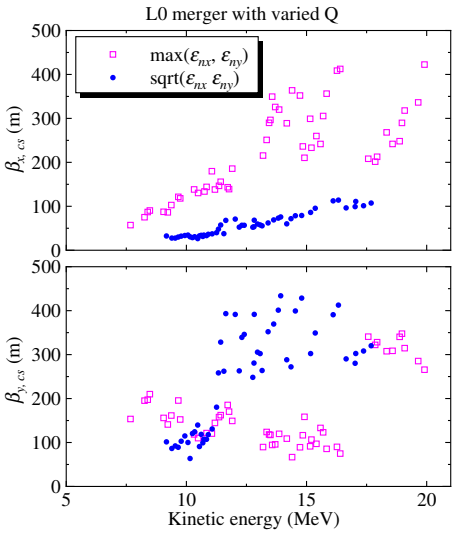

Figure 60: $\beta_{x,cs}$ and $\beta_{y,cs}$ of Courant-Snyder parameters at end of beamline. The horizontal axis is same as Fig. 55.

2.8 Summary

In order to study emittance growth in merger section, optimizations of beamline parameters were carried out using particle tracking code, GPT. In the simulation, a beam with 80 pC bunch charge was tracked in beamlines. As beamlines to study the emittance growth, we used L0B1 merger, which consists of three dipole magnets and two quadrupole magnets, zigzag merger, which consists of four dipole magnets, and pure drift space to compare emittance growth caused by space charge effect alone. The beamlines have two sections, merger section and main SRF section, which consists of five super conducting RF cavities. In order to improve accuracy of space charge calculation in merger section, we developed enhanced space charge routine based on mesh method for GPT. In the optimization, two beam parameters were minimized by multi-objective method. They are transverse emittance and rms bunch length or kinetic energy at the exit of the beamline. To estimate the transverse emittance, max(ϵ_{nx}, ϵ_{ny}) or sqrt($\epsilon_{nx}\epsilon_{ny}$) was used as the one of objective in the optimization. From the results to minimize max(ϵ_{nx}, ϵ_{ny}) and bunch length, emittance growth in pure drift beamline is estimated to be less than 0.1 mm mrad. The results in the zigzag merger are less than the results in the L0B1 merger. It shows that the nontrivial achromatic condition for longitudinal linear space charge in zigzag merger is effective to reduce emittance growth in merger section. For bunch length of 0.8 mm at the end of beamline, the emittances at the end of beamline for L0B1 with fixed quadrupoles, L0B1 with varied quadrupoles, zigzag and pure drift are 0.338, 0.297, 0.231 and 0.052 mm mrad, respectively. However, to adjust the quadrupole strengths in L0B1 merger section, the emittance growth for L0B1 merger can approach one for zigzag merger. In addition, L0B1 merger has advantage for layout of beamline. Therefore, L0B1 merger is better than other types of merger for Cornell University ERL.

For minimizing max(ϵ_{nx}, ϵ_{ny}), the horizontal emittance is almost same as the vertical emittance. On the other hand, the difference between the horizontal and vertical emittances for minimizing sqrt($\epsilon_{nx}\epsilon_{ny}$) is larger than one for minimizing max(ϵ_{nx}, ϵ_{ny}). In this case, the vertical emittance is extremely small same as one for pure drift, and the horizontal emittance is extremely large, and is distributed from 0.6 to 2.5 mm mrad. In actual beam operation, it is required that the both horizontal and vertical emittances are smaller. Therefore, minimizing max(ϵ_{nx}, ϵ_{ny}) is better to optimize beamline parameters.

In order to study effect of initial kinetic energy at entrance of merger section, optimizations to minimize max(ϵ_{nx}, ϵ_{ny}) or sqrt($\epsilon_{nx}\epsilon_{ny}$) and initial kinetic energy were carried out. Since space charge effect becomes weaker for higher initial energy, the emittance growth decreases depended on initial energy. For 20 MeV initial kinetic energy, the emittance growth is less than 0.05 mm mrad. The results of the optimization to minimize emittance and initial kinetic energy shows that the initial kinetic energy before the merger section is very important to reduce the emittance growth in the merger section.

3 CSR effect in merger

Both ERLs and FELs require electron bunches of low emittance and short duration for production of high quality synchrotron radiation. The optimization of various parameters to suppress emittance growth due to the space charge effects at low energy in a DC gun based photoinjector has been carried out using a space charge code ASTRA [1, 2]. Additionally, the effects of space charge and CSR on beam dynamics in an ERL merger must be carefully considered. The usual 1D treatment of CSR [6], however, assumes ultrarelativistic electron beam energies, and therefore cannot be applied to low energy transport lines typical for ERL injection system. Full accounting of space charge and CSR forces requires self-consistent solution to Lienard-Wiechert potentials [7, 8], in turn leading to CPU-time expensive calculations, which are of limited use in extensive optimizations necessary in obtaining ultimate performance of an injector. Alternatively, in order to investigate the beam dynamics in a full injector, we have developed and implemented a new CSR routine, GPT/CSR [9], for a particle tracking code, GPT [3], which includes efficient 3D space charge effect treatment based on nonequidistant multigrid Poisson solver. GPT/CSR does not assume ultrarelativistic electron beam [4, 5], and is therefore effective for the merger or chicane simulations at low energies where both CSR and space charge may be important at the same time.

We summarize changes to GPT code that extend its applicability to treatment of space charge and CSR effects in the bends at low energy.

3.1 CSR calculation in GPT

The CSR routine calculates 1D CSR wake based on the formalism of Sagan [4, 5]. The formalism does not assume ultrarelativistic electron beam making it effective at low energies. Furthermore, the CSR routine correctly calculates transient wake-fields for arbitrary beam trajectories, which are stored in parametric form for the purpose of retarded time calculations, etc. Besides, the routine can calculate the effects of vacuum chamber shielding using image charges.

3.2 Energy Loss and Spread

The steady-state energy loss and spread for various beam energies are compared as calculated by GPT/CSR, `elegant`, and analytical expression for a circular orbit with the bending radius of $\rho = 1.0\,\mathrm{m}$. In the calculation, the bunch length is $\sigma_s = 0.6\,\mathrm{mm}$, the initial distribution is Gaussian, and the bunch charge is -80 pC. Figures 61 and 62 show the energy loss $d\varepsilon/dt$ and incremental energy spread $d\sigma_\delta/dt$ respectively for the steady-state case. The red line in Fig. 61 is the analytical result derived by C. Mayes [10],

$$\frac{d\varepsilon}{dt} = -\frac{2}{3}\frac{(r_e m_e c^2) c\beta^4\gamma^4}{\rho^2} N\left(1 + (N-1)T(a)\right), \tag{47}$$

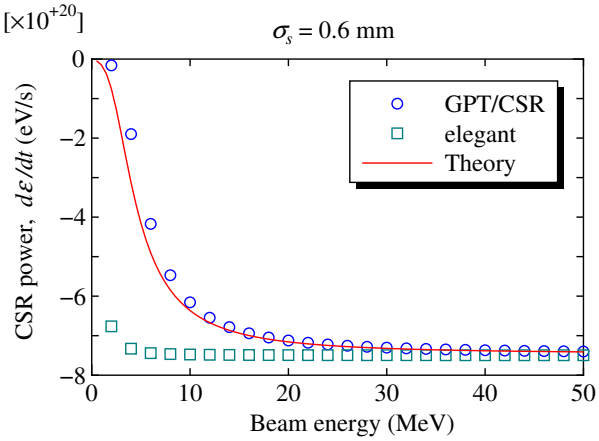

Figure 61: Steady-state energy loss for a circular orbit with $\rho = 1\,\mathrm{m}$.

where $a = 3/2 \cdot \gamma\ 3\sigma_s/(\beta\rho)$,

$$T(a) = \frac{9}{32\pi}\frac{1}{a^3}\left(\mathrm{e}^{\frac{1}{(8a^2)}}\sqrt{\pi}K_{5/6}\left(\frac{1}{8a^2}\right) - 2\pi a\right), \tag{48}$$

$K_{5/6}(x)$ is the modified Bessel function, N is the number of electrons in the bunch, m_e is the electron mass, r_e is the classical electron radius, c is the speed of light, γ is the Lorentz energy factor and $\beta = (1 - 1/\gamma^2)^{1/2}$. The agreement between `elegant` and the theory is good only for higher beam energy, $E_0 > 40$ MeV because the CSR routine in `elegant` includes the assumption of ultrarelativistic beam [6]. On the other hand, GPT/CSR reproduces the analytical result accurately, as seen in Fig. 61.

The red line in Fig. 62 is the analytical result [11, 12], which includes the assumption of $\gamma >> (\rho/\sigma_s)^{1/3}$,

$$\frac{d\sigma_\delta}{dt} \approx 0.22\frac{r_e N c\beta}{\gamma\rho^{2/3}\sigma_s^{4/3}}. \tag{49}$$

Fig. 62 shows that the results of GPT/CSR and `elegant` both reproduce well the analytical result for higher beam energy, $E_0 > 40$MeV. However, the results of `elegant` and the theory diverge to infinity for $E_0 \to 0$ unlike GPT/CSR, which approaches zero as expected.

These results show that the GPT/CSR is effective for wide range of beam energies, and can be used to investigate beam dynamics in ERL and FEL photoinjectors.

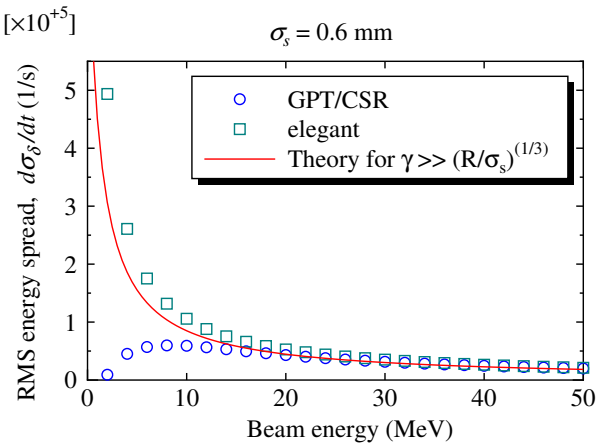

Figure 62: Steady-state incremental rms energy spread for a circular orbit with $\rho = 1\,\mathrm{m}$.

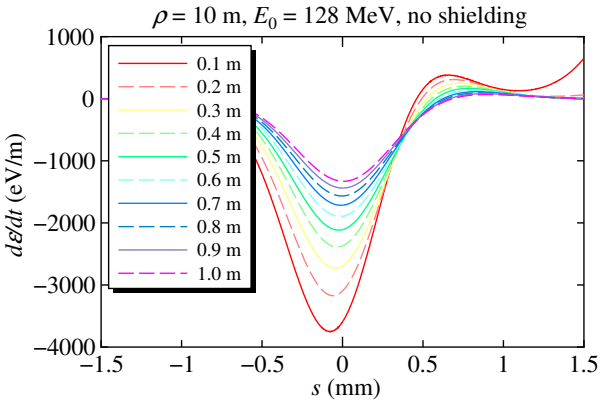

Figure 63: CSR wake without shielding from the end of bending magnet. The bunch length is 0.3 mm.

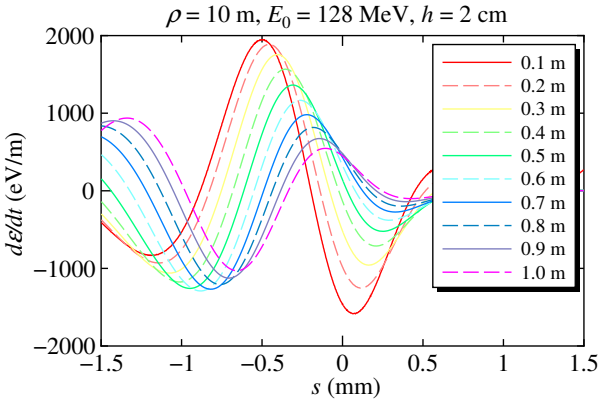

Figure 64: CSR wake with shielding from the end of bending magnet. The shielding chamber height is 2 cm.

3.3 CSR in Transient State

An example of CSR effect in a transient state, the CSR wake form is calculated by GPT/CSR after the exit of a bending magnet for the following parameters: the beam energy 128 MeV, Gaussian particle distribution, the bunch length 0.3 mm, and the bunch charge −80 pC. Figures 63 and 64 show the transient CSR wake with and without shielding included. In Fig. 64, the shielding chamber height and the number of image charge layers are 2 cm and 32, respectively. Before the start point, $\Delta s = 0$ m, the bunch moves in a bending magnet of bending radius $\rho = 10$ m having reached a steady-state CSR condition. After the starting point, the bunch moves in a drift space. The figures show that the CSR wake reduces as the distance from the exit of the bending magnet increases as expected.

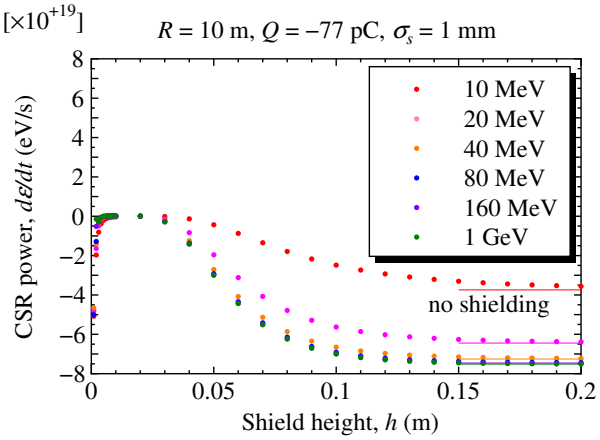

Figure 65: Energy loss for various shield heights in a steady-state case. The number of image charges is 32.

3.4 CSR Shielding Effect

The effect of CSR shielding is calculated by GPT/CSR for a circular orbit of a bending radius, $\rho = 10$ m. Figure 65 shows the energy loss for various shield heights in a steady-state case. In the calculation, the initial particle distribution is Gaussian, the bunch length is 1.0 mm, the bunch charge is -80 pC, and the number of image charges is 32. The solid lines in Fig. 65 are the analytical values without the shielding as calculated by Eq. (47). As the shielding height increases, the energy loss approaches to the analytical value.

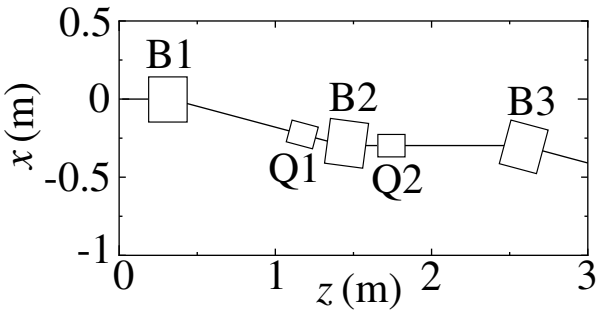

Figure 66: Layout of 3 dipoles merger in Cornell University.

3.5 CSR in Merger Section

As an example, the transverse emittance in a 3-dipole merger of ERL project at Cornell University is calculated by GPT/CSR and `elegant` for three different conditions, (a) $p_0 = 10$ MeV/c without CSR, (b) $p_0 = 10$ MeV/c with CSR, (c) $p_0 = 500$ MeV/c with CSR. Space charge calculations have been suppressed in GPT for this example. The layout of the merger is shown in Fig. 66, which consists of three bending magnets and two quadrupoles. Figure 67 shows the evolutions of the normalized horizontal emittance as a function of longitudinal position. Figure 68 shows the evolution of the horizontal rms beam size. The bunch length is 0.3 mm, the particle distribution is Gaussian. For Fig. 67 (b) $p_0 = 10$ MeV/c, the GPT/CSR and `elegant` results disagree. On the other hand, for Fig. 67 (a) $p_0 = 10$ MeV/c with CSR and (c) $p_0 = 500$ MeV/c with CSR, the agreement is good demonstrating that GPT/CSR reproduces `elegant` CSR calculations at higher beam energies as expected.

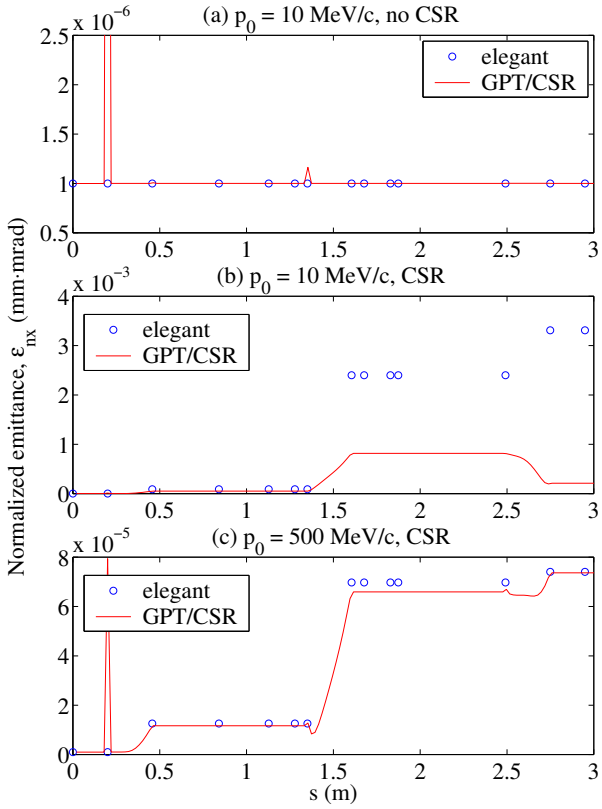

Figure 67: Normalized emittance in 3 dipoles merger of Fig. 66 calculated by `elegant` and GPT/CSR.

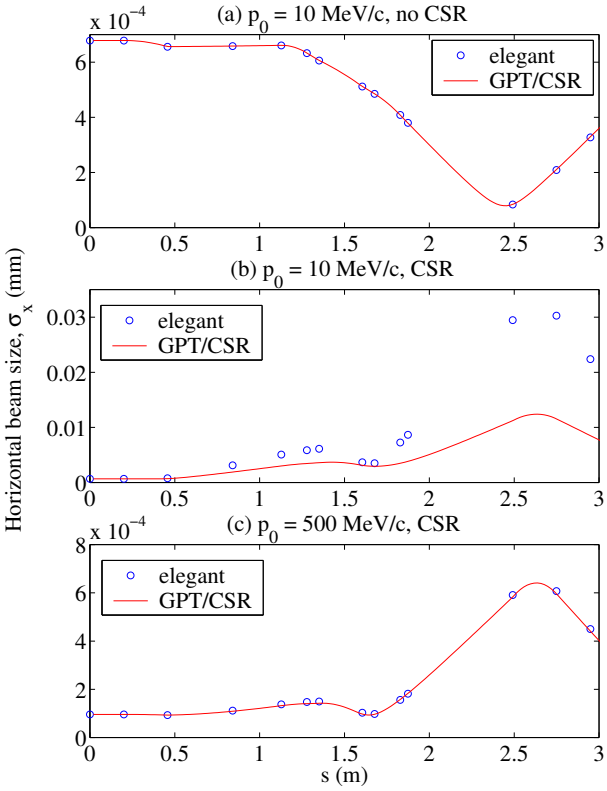

Figure 68: Horizontal rms beam size in the merger of Fig. 66 calculated by `elegant` and GPT/CSR.

3.6 Emittance growth caused by space charge effect and CSR

In order to estimate emittance growth in merger section caused by space charge effect and CSR, simulations with CSR were carried out using GPT/CSR. As a beamline, L0B1 merger was used. To compare the results with and without CSR, optimized beamline parameters for L0B1 merger with varied Qs as shown in Figure 35 and Figure 55 were used as beamline parameters. Conditions in the simulations were same as the conditions described in section 2.

In addition, to estimate effect of CSR shielding, simulations with and without CSR shielding were carried for same beamline parameter. In the simulation with CSR shielding, number of image charge layer was 16 layers, and height of vacuum chamber was 2 cm.

3.6.1 Minimize max$(\epsilon_{nx}, \epsilon_{ny})$ and σ_z

In the simulations, initial kinetic enegy and bunch charge were fixed to be 10 MeV and 80 pC, respectively. Figure 69 shows results with CSR effect to minimize max$(\epsilon_{nx}, \epsilon_{ny})$ and σ_z. The horizontal axis is same as Figure 35. As shown in Figure 69, the effect of CSR are extremely small compared with emittance growth caused by space charge effect. Although CSR effect is stronger for shorter bunch length beam, the differences are extremely small for initial energy of 10 MeV. Figure 70 shows horizontal and vertical emittances. Horizontal and vertical rms beam size at end of beamline are shown in Figure 71. Figure 72 shows the kinetic energy and rms energy spread at the end of beamline. These graphs show that the CSR effect can be neglected in L0B1 merger.

For bunch length of 0.8 mm, time evolutions emittances, beam sizes, kinetic energy and rms energy spread are shown in Figures 73, 74 and 75. The little difference of horizontal emittance between with and without shielding were observed before the main SRF section. However, after the acceleration by main SRF cavities, the difference becomes smaller. The differences of other parameters were extremely small.

The results show that although the difference of horizontal emittance caused by CSR effect before mein SRF section is observed, it is extremely small, and we can neglect CSR effect in L0B1 merger with 10 MeV electron beam.

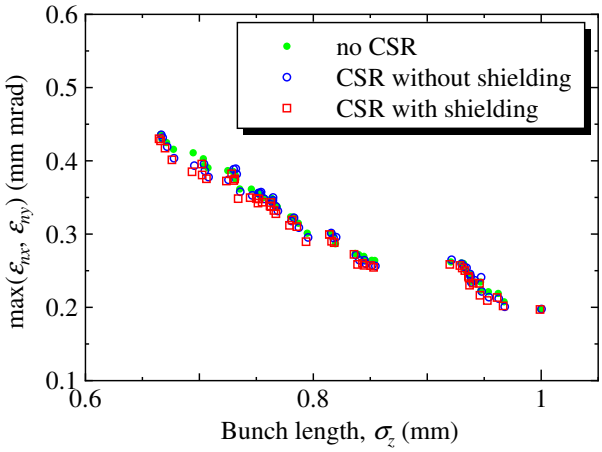

Figure 69: Optimization results with CSR effect to minimize $\max(\epsilon_{nx}, \epsilon_{ny})$ and σ_z. The horizontal axis is same as Figure 35. The results with out CSR is same as the results for L0B1 merger with varied Q in Figure 35.

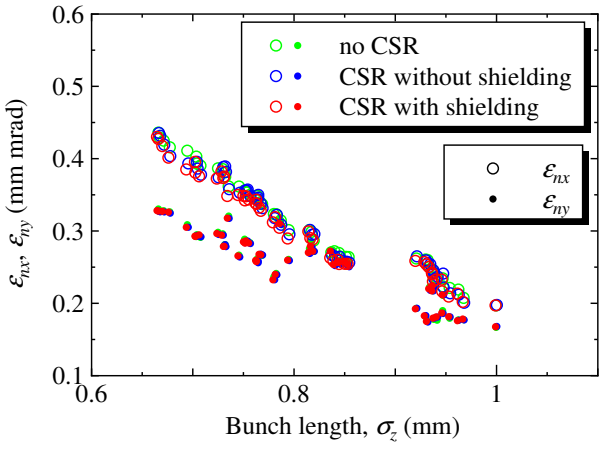

Figure 70: Horizontal and vertical normalized rms emittances at end of beamline. The horizontal axis is same as Figure 35. The results with out CSR is same as the results for L0B1 merger with varied Q in Figure 36.

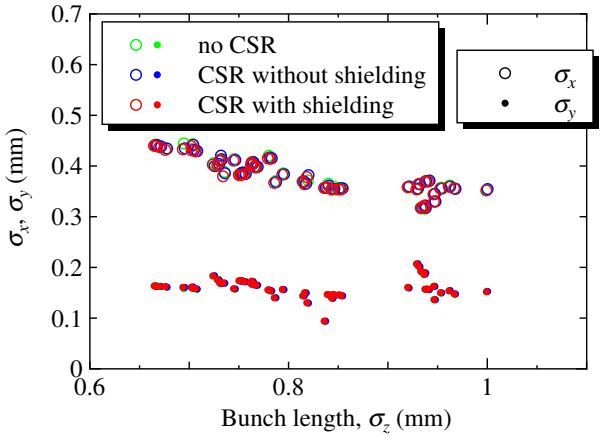

Figure 71: Horizontal and vertical rms beam size at end of beamline. The horizontal axis is same as Figure 35. The results with out CSR is same as the results for L0B1 merger with varied Q in Figure 37.

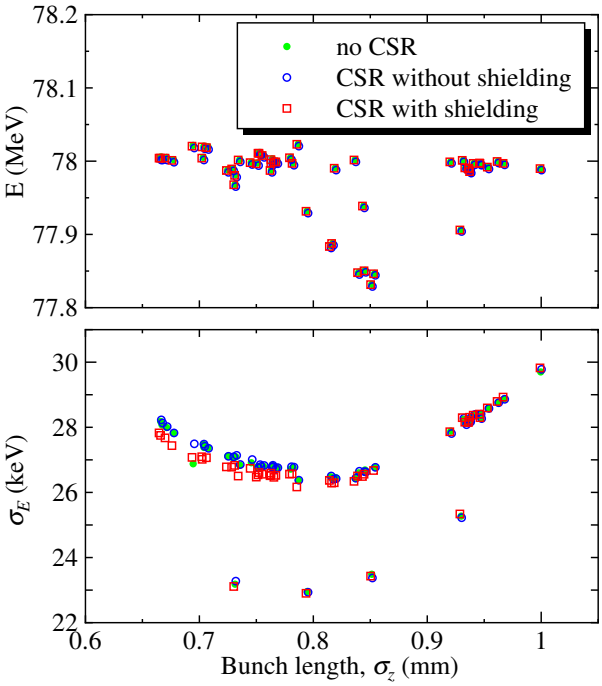

Figure 72: Kinetic energy and rms energy spread at end of beamline. The horizontal axis is same as Figure 35. The results with out CSR is same as the results for L0B1 merger with varied Q in Figure 38.

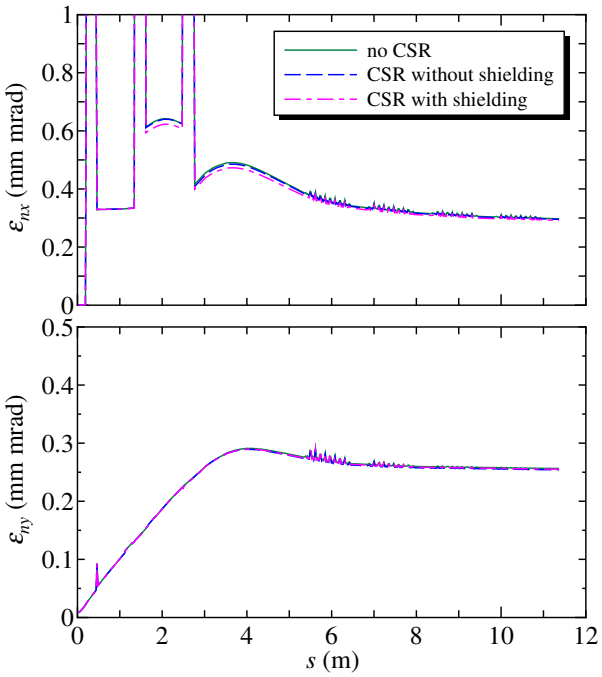

Figure 73: Time evolutions of normalized rms emittances in L0B1 beamline with varied quadrupole magnets and CSR effect. The optimized beamline parameters with the bunch length of 0.8 mm at the end of beamline are shown in Table 15. The results with out CSR is same as the results for L0B1 merger with varied Q in Figure 44.

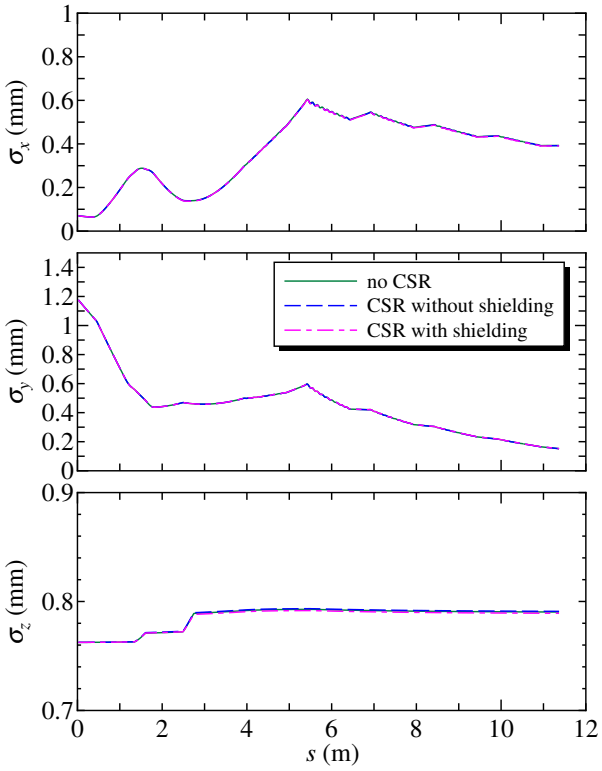

Figure 74: Time evolutions of transverse rms beam sizes and bunch length with optimized beamline parameters. The results with out CSR is same as the results for L0B1 merger with varied Q in Figure 44.

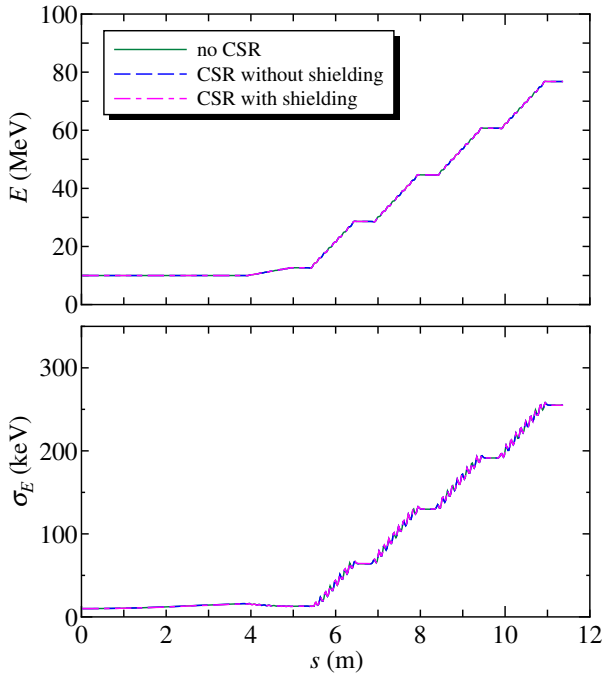

Figure 75: Time evolutions of kinetic energy and rms energy spread with optimized beamline parameters. The results with out CSR is same as the results for L0B1 merger with varied Q in Figure 46.

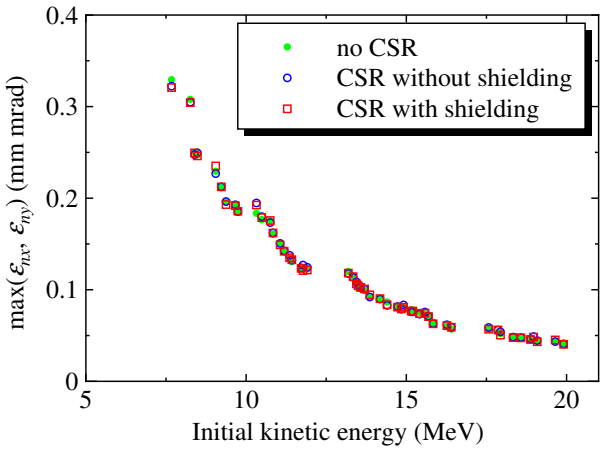

Figure 76: Optimization results with CSR effect to minimize $\max(\epsilon_{nx}, \epsilon_{ny})$ and initial kinetic energy, E. The horizontal axis is same as Figure 55. The results with out CSR is same as the results for L0B1 merger with varied Q in Figure 55.

3.6.2 Minimize emittance and initial kinetic energy

In the simulations, initial bunch length and bunch charge were fixed to be 0.9 mm and 80 pC, respectively. Figure 76 shows results with CSR effect to minimize $\max(\epsilon_{nx}, \epsilon_{ny})$ and initial kinetic energy, E. The figure shows that the effect of CSR is negligible in the energy range from 7.5 to 20 MeV. Figures 77, 78 and 79 show transverse emittances, transverse emittances, kinetic energy and rms energy spread, respectively. These figures show that the CSR effect in L0B1 merger is extremely small. Therefore, in calculation of emittance growth in L0B1 merger, space charge effect is dominant, and CSR effect is negligible.

3.7 Summary

In order to study CSR effect in merger section, we developed a CSR routine, GPT/CSR. In merger section, typical beam energy is 10 MeV, and it is lower compared with beam energy in return loop. Thus, accurate CSR calculation in lower energy region is required for the GPT/CSR. Comparing results calculated by the GPT/CSR with analytical expression and numerical results calculated by `elegant`, we confirmed the GPT/CSR is effective for wide range of beam energies, and can be used to investigate beam dynamics in ERL and FEL photoinjectors.

To estimate the emittance growth caused by CSR in merger section, particle tracking simulations with space charge and CSR effect were carried out using the GPT/CSR. The results shows that space charge effect is dominant, and CSR effect is negligible in calculation of emittance growth in L0B1 merger. However, in the future, to generate shorter bunch length beam with higher energy, CSR effect in the merger section may become important.

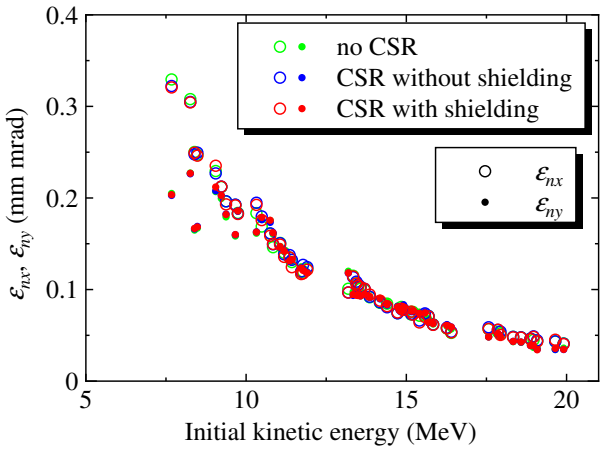

Figure 77: Horizontal and vertical normalized rms emittances at end of beamline. The horizontal axis is same as Figure 55. The results with out CSR is same as the results for L0B1 merger with varied Q in Figure 56.

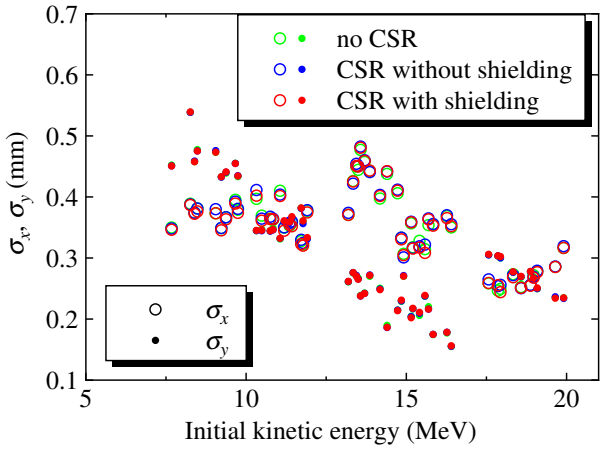

Figure 78: Horizontal and vertical rms beam size at end of beamline. The horizontal axis is same as Figure 55. The results with out CSR is same as the results for L0B1 merger with varied Q in Figure 57.

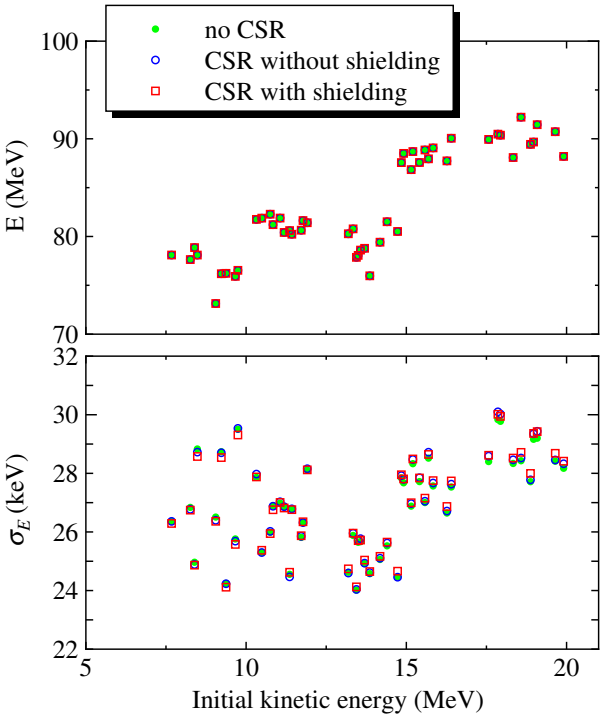

Figure 79: Kinetic energy and rms energy spread at end of beamline. The horizontal axis is same as Figure 55. The results with out CSR is same as the results for L0B1 merger with varied Q in Figure 58.

A Achromatic condition

Decoupling condition between transverse and longitudinal motions in merger was derived by Kayran [13]. Here, in order to introduce the decoupling condition with longitudinal space charge force, we describe normal achromatic condition.

Horizontal betatron motion in focusing system is given by a homogeneous equation,

$$X'(s) = D(s)X(s), \tag{50}$$

where $'$ denotes d/ds, and s is a longitudinal coordinate along the orbit of reference particle. The horizontal phase space coordinate is

$$X(s) = \begin{pmatrix} x(s) \\ x'(s) \end{pmatrix}, \tag{51}$$

where $x(s)$ is the particle coordinate from the reference particle, and $x'(s) = dx/ds$. $D(s)$ is given by

$$D(s) = \begin{pmatrix} 0 & 1 \\ -K_1(s) & 0 \end{pmatrix}, \tag{52}$$

where $K_1(s)$ is focusing (defocusing) strength.

We consider a transverse particle motion with an energy deviation, $\delta(s)$. Then, the equation of motion is given by

$$x''(s) = -K_1(s)x + \frac{1}{\rho(s)}\delta(s), \tag{53}$$

where $\rho(s)$ is the bending radius of the trajectory defined by the dipole magnetic field, and the curvature of the trajectory is $K_o(s) = 1/\rho(s)$. The energy deviation is defined by $\delta = (E - E_o)/p_o c$, where E and E_o are energies of the particle and the reference particle, respectively. p_o is the momentum of the reference particle. The equation of motion can be described by

$$X'(s) = D(s)X(s) + \delta(s) \begin{pmatrix} 0 \\ K_o(s) \end{pmatrix}. \tag{54}$$

This is an inhomogeneous differential equation. In order to obtain the general solution of the equation, the traditional variation method for ordinary linear differential equation is used. For the homogeneous equation (50), the solution becomes

$$X(s) = M(s_0|s)X(s_0), \tag{55}$$

where $M(s_0|s)$ is the transport matrix. It satisfies the linear equation of motion (50),

$$M'(s_0|s) = D(s)M(s_0|s). \tag{56}$$

Here, we assume that the inhomogeneous equation (54) has a solution,

$$X(s) = M(s_0|s)A(s). \tag{57}$$

Substituting it for Eq. (54), we obtain

$$A'(s) = \delta(s) K_o(s) M^{-1}(s_0|s) \begin{pmatrix} 0 \\ 1 \end{pmatrix}. \tag{58}$$

After the integration of $A'(s)$ from s_0 to s, the function, $A(s)$, becomes

$$A(s) = A(s_0) + \int_{s_0}^{s} \delta(s_1) K_o(s_1) M^{-1}(s_0|s_1) \begin{pmatrix} 0 \\ 1 \end{pmatrix} ds_1. \tag{59}$$

Therefore, the general solution of the inhomogeneous equation (54) becomes

$$\begin{aligned} X(s) &= M(s_0|s) \cdot \\ &\quad \left\{ X(s_0) + \int_{s_0}^{s} \delta(s_1) K_o(s_1) M^{-1}(s_0|s_1) \begin{pmatrix} 0 \\ 1 \end{pmatrix} \right\}. \end{aligned} \tag{60}$$

For $\delta(s) = 0$, it becomes $X(s) = M(s_0|s)X(s_0)$. The second term in the right hand side is the coupling term between the longitudinal and the transverse motions. When the second term in the right hand side is zero at the exit of merger, the condition becomes achromatic. From Eq. (60) and

$$M(s_0|s) = \begin{pmatrix} m_{11}(s_0|s) & m_{12}(s_0|s) \\ m_{21}(s_0|s) & m_{22}(s_0|s) \end{pmatrix}, \tag{61}$$

generalized dispersion is defined by

$$R(s) = \begin{pmatrix} I_1(s) \\ I_2(s) \end{pmatrix}, \tag{62}$$

where

$$I_1(s) = \int_{s_0}^{s} \delta(s_1) K_o(s_1) m_{12}(s_1|s) ds_1, \tag{63}$$

$$I_2(s) = \int_{s_0}^{s} \delta(s_1) K_o(s_1) m_{22}(s_1|s) ds_1. \tag{64}$$

Here, the relation of the transform matrix,

$$M(s_0|s) M^{-1}(s_0|s_1) = M(s_1|s), \tag{65}$$

was used. Using the generalized dispersion, Eq. (60) can be described by

$$X(s) = M(s_0|s) X(s_0) + R(s). \tag{66}$$

Specific solution for $\delta(s) = 1$ gives the transverse dispersion function,

$$\begin{aligned} \eta_x(s) &= \int_{s_0}^{s} K_o(s_1) m_{12}(s_1|s) ds_1 \\ &= m_{12}(s_0|s) I_c(s) - m_{11}(s_0|s) I_s(s), \end{aligned} \tag{67}$$

and

$$\begin{aligned}\eta_x'(s) &= \int_{s_0}^{s} K_o(s_1) m_{22}(s_1|s) ds_1 \\ &= m_{22}(s_0|s) I_c(s) - m_{21}(s_0|s) I_s(s). \end{aligned} \tag{68}$$

Here, $I_c(s)$ and $I_s(s)$ are defined by

$$I_c(s) = \int_{s_0}^{s} K_o(s_1) m_{11}(s_0|s_1) ds_1, \tag{69}$$

$$I_s(s) = \int_{s_0} s K_o(s_1) m_{12}(s_0|s_1) ds_1. \tag{70}$$

And, the relationships of transport matrix,

$$\begin{aligned} m_{12}(s_0|s) &= -m_{11}(s_0|s) m_{12}(s_0|s_1) \\ &\quad + m_{12}(s_0|s) m_{11}(s_0|s_1), \end{aligned} \tag{71}$$

$$\begin{aligned} m_{22}(s_1|s) &= -m21(s_0|s) m_{12}(s_0|s_1) \\ &\quad + m_{22}(s_0|s) m_{11}(s_0|s_1), \end{aligned} \tag{72}$$

which were derived from $M(s_0|s)M^{-1}(s_0|s_1)$, were used to define $I_c(s)$ and $I_s(s)$. The conventional achromatic conditions at the exit of merger, $z = s_f$, are described by

$$\eta_x(s_f) = 0, \tag{73}$$

$$\eta_x'(s_f) = 0, \tag{74}$$

or using $I_c(s)$ and $I_s(s)$,

$$I_c(s_f) = 0, \tag{75}$$

$$I_s(s_f) = 0. \tag{76}$$

References

[1] I. V. Bazarov and C. K. Sinclair, Phys. Rev. ST Accel. Beams **8**, 034202 (2005).

[2] K. Floettmann, ASTRA.

[3] Pulsar Physics, http://www.pulsar.nl/gpt/index.html

[4] D. Sagan, *Proceedings of EPAC06*, Edinburgh, Scotland, 2006, pp. 2829-2831.

[5] David Sagan, Georg Hoffstaetter, Christopher Mayes, and Udom Sae-Ueng, Phys. Rev. ST Accel. Beams **12**, 040703 (2009).

[6] M. Borland, Phys. Rev. ST-AB **4**, 070701 (2001).

[7] L. Giannessi, P. Musumeci, and M. Quattromini, NIM A **436**, 443 (1999).

[8] M. Dohlus, A. Kabel and T. Limberg, NIM A **445**, 338 (2000).

[9] I. V. Bazarov and T. Miyajima, *Proceedings of EPAC08*, Genoa, Italy, 2008, pp. 118-120.

[10] C. Mayes, private communication.

[11] P. Emma and R. Brinkmann, *Proceedings of PAC97*, Vancouver, B.C., Canada, 1997, pp. 1679-1681.

[12] Ya. S. Derbenev. *et.al.*, TESLA FEL-Report 1995-05.

[13] Vladimir N. Litvinenko, Ryoichi Hajima, and Dmitry Kayran, NIM A **557**, 165 (2006).